A Symplectic Numerical Power Flow Framework Based on Wave Finite-Element Method for Assembled Structural Systems

Wave-Based Power Flow Method Using the Zhong–Williams Scheme for Periodic and Assembled Structures

Abstract

This paper presents a guided-wave power flow calculation method based on the Zhong–Williams scheme. A numerically stable power orthogonality between wave modes is established based on symplectic orthogonality (SO) and symplectic adjoint orthogonality (SAO), and subsequently extended to the Zhong–Williams eigenvalue problem. This leads to a generalized symplectic adjoint orthogonality (GSAO), which enables the formulation of transfer relations between eigenvectors of adjacent periodic substructures. These developments enable the Zhong–Williams scheme to independently compute both the forced response and the associated power flow. Four power flow calculation methods within the wave finite element (WFE) framework, including the Mead scheme, are summarized and validated on a beam and a cylindrical shell. An assembled electric motor housing is used as a case study, in which the proposed approach establishes a wave-mode power flow network. The network reveals the dominant energy transmission paths and a localized energy circulation from a wave-based perspective. The method provides theoretical support for wave-informed energy regulation and vibration control in complex assembled structures.

Keywords: Zhong-Williams scheme, symplectic orthogonality, power flow, guided wave, wave finite element method

1. introduction

Guided waves provide an intrinsic perspective for understanding structural vibration and acoustics. A sound knowledge of guided waves is crucial for the accurate comprehension of their propagation features, including dispersion relations, wave shapes, power flow, and scattering/diffraction. This

facilitates the application of guided waves in many areas such as vibration suppression [1, 2], structural health monitoring [3, 4, 5], and acoustic metamaterials [6, 7].

Analytical formulations have been developed to derive dispersion relations in plate and cylindrical structures. A common approach to deriving the dispersion relation is to assume a time-harmonic and spatially sinusoidal displacement field, which transforms the elastodynamic equations into a frequency–wavenumber relation under appropriate boundary conditions [8, 9]. For isotropic plates, Lamb [10] derived such a relation in 1917 based on time-harmonic motion under plane strain and traction-free boundary conditions, leading to a transcendental dispersion equation later evaluated numerically by Gazis et al. in 1958 [11]. This formulation was later generalized to multilayered and anisotropic plates by expressing closed-form solutions within each layer and imposing continuity of displacements and tractions at the interfaces, yielding transcendental dispersion relations solvable via state-space or stabilized transfer matrix methods [12, 13, 14]. For cylindrical shell structures, the seminal work by Leissa provides a comprehensive review of the acoustic characteristics of various shell types, including thin/thick shells and open shells [15]. For certain anisotropic cylindrical shells, the displacement fields are expanded using Chebyshev or Legendre polynomials instead of Fourier series, enabling better representation of high-order coupling and localized variations under complex boundary conditions [16, 17]. While these analytical approaches remain effective for regular configurations, waveguide geometries that involve discontinuities, such as damage, joints, or geometric complexities, often require the development of numerical methods.

The wave finite element method (WFEM) is a mature numerical approach for computing dispersion relations in periodic structures [18, 19]. It requires only a finite element model of the unit cell, the smallest repeatable substructure, whose dynamic stiffness matrix can be obtained via commercial software and transformed into a transfer matrix [20]. Solving its eigenvalue problem yields both wave vectors and mode shapes. However, this transformation involves inverting a block matrix, which may cause numerical instability even when the matrix is theoretically invertible [21]. To overcome this, Mead proposed a quadratic eigen-problem based on displacement continuity and force equilibrium, avoiding matrix inversion and improving stability for systems with many degrees of freedom (DOFs) [22, 23]. Yet, the presence of strongly evanescent waves can still lead to extreme eigenvalues and poor conditioning [24]. Zhong and Williams addressed this by formulating a generalized

symplectic eigen-problem, which pairs eigenvalues of oppositely propagating waves and improves numerical conditioning [25, 26]. The transfer matrix, Mead, and Zhong–Williams schemes are the three most widely used formulations in WFEM. Solutions to additional numerical issues, including balancing strategies and repeated root handling, are detailed in [27, 28, 29]. With advances in numerical precision and eigenvalue solvers, WFEM has become a robust tool for dispersion analysis.

Beyond dispersion analysis, WFEM has been extensively extended to address forced responses, wave scattering introduced by coupling element, and power flow. This extension relies on the principle that structural vibrations result from wave propagation and superposition, reflecting wave–vibration consistency [30]. To relate external excitations to wave domain, many studies formulate system-level input–output relations in terms of equivalent impedance matrices, which can be traced back to the foundational work of Duhamel et al. [31, 32]. This approach significantly reduces computational costs, particularly for large periodic systems, as structural responses are represented in the wave domain where the transfer matrix becomes diagonalizable, allowing mode-wise propagation to be computed independently. Comparing forced responses with commercial finite element results has become a standard practice for validating in-house implementations. Moreover, recent developments have extended WFEM to the time domain, where frequency-domain impedance matrices are recast into second-order differential equations via rational approximation, enabling the computation of transient responses through standard time integration schemes such as the Newmark method [33, 34].

To further accommodate structural discontinuities and localized coupling features, researchers developed the diffusion matrix method (DMM), a hybrid strategy that integrates FE and wave-based modeling [35, 36]. In this method, complex coupling components are retained in the physical domain using FE modeling, while their interfaces with adjoining waveguides are projected onto the wave basis. This enables the construction of a diffusion matrix that directly relates incident and transmitted wave amplitudes, allowing efficient evaluation of wave-mode conversions. Subsequently, various model reduction techniques were incorporated into the DMM framework to further improve computational efficiency [37]. The DMM has been applied to a range of wave scattering problems. Huang et al. and Zhou et al. analyzed its use in damaged stiffened plates and locally defective pipes respectively, demonstrating the sensitivity of specific wave modes to joint damage

and highlighting the potential of multi-mode strategies for structural health monitoring [38, 39]. Renno and Mace further generalized the formulation to tackle wave scattering from multiple joints within structural networks [40]. Fan et al. treated the excitation source as an embedded joint, investigating wave attenuation in damped systems and examining energy redistribution among wave modes both inside and outside bandgap regions [41].

In addition to its efficiency in modeling wave scattering, WFEM also facilitates the evaluation of wave-mode power flow, as it provides direct access to displacement and force components for each wave mode [41, 42]. The power carried by each mode can be conveniently computed from the wave solutions using standard formulas involving stress and displacement [29]. Particularly, power flow provides a coherent and directional representation of energy transmission, mode conversion, and localized circulation within complex structures—features that are not readily observable through displacement fields alone. These capabilities make power flow particularly valuable in analyzing multi-interface or heterogeneous systems where energy redistribution mechanisms are of interest.

However, existing computation of forced response and power flow are largely based on the Mead scheme. Although the Zhong–Williams scheme offers better numerical stability, its eigensolutions lie in a generalized symplectic space, where the eigenvectors lack direct physical interpretation and cannot be transferred across unit cells. As such, they are typically projected back into the wave space for propagation, effectively reverting to the Mead framework [27]. Furthermore, unlike the modal orthogonality of dynamic stiffness matrices, the skew symmetry of the transfer matrix leaves the power orthogonality between wave modes insufficiently understood, which often prevents a complete decoupling of wave modes.

This study introduces a power flow computation method based on the Zhong–Williams scheme. Power orthogonality between wave modes is established via symplectic orthogonality (SO) and symplectic adjoint orthogonality (SAO), providing a numerically stable foundation for modal decoupling. A transfer relation is then derived within the generalized symplectic eigenspace, enabling direct computation of forced response and power flow without reverting to the wave space. The accuracy and robustness of the proposed method are validated numerically. Four WFEM-based power flow formulations are further summarized, and an assembled electric motor housing is analyzed to illustrate substructural power flow and the global energy transmission network from a wave-mode perspective.

The paper is organized as follows. Section 2 outlines the wave finite element framework, covering eigenvalue schemes, forced response, and power flow. Section 3 derives the power orthogonality and the wave-mode propagation relation, and extends both to the Zhong–Williams scheme to derive formulations for forced response and power flow. Section 4 evaluates the numerical stability and accuracy of the proposed method through applications to beam and shell structures. Section 5 applies the approach to a assembled structure to construct the wave-mode power flow network.

2. Wave finite element method

2.1. Eigenvalue schemes

2.1.1. transfer matrix scheme

A schematic of a typical periodic structure is shown in Fig. 1. The structure can be efficiently modeled in commercial finite element software using a single unit cell. While the internal meshing of the unit cell is arbitrary, a one-to-one correspondence between nodes on the left and right boundaries needs to be preserved to ensure continuity across adjacent cells. The dynamic stiffness matrix of this model is written as

$$\begin{bmatrix} \boldsymbol{D}_{\mathrm{LL}} & \boldsymbol{D}_{\mathrm{LR}} & \boldsymbol{D}_{\mathrm{LI}} \\ \boldsymbol{D}_{\mathrm{LR}} & \boldsymbol{D}_{\mathrm{RR}} & \boldsymbol{D}_{\mathrm{RI}} \\ \boldsymbol{D}_{\mathrm{IL}} & \boldsymbol{D}_{\mathrm{IR}} & \boldsymbol{D}_{\mathrm{II}} \end{bmatrix} \begin{bmatrix} \boldsymbol{q}_{\mathrm{L}} \\ \boldsymbol{q}_{\mathrm{R}} \\ \boldsymbol{q}_{\mathrm{I}} \end{bmatrix} = \begin{bmatrix} \boldsymbol{f}_{\mathrm{L}} \\ \boldsymbol{f}_{\mathrm{R}} \\ \boldsymbol{f}_{\mathrm{I}} \end{bmatrix} \tag{1}$$

where the subscripts L, R, and I denote the left, right and internal boundaries, respectively; $\boldsymbol{q}$ and $\boldsymbol{f}$ represent the displacement and force components. Since the internal nodes are not subjected to external forces, their DOFs can be statically condensed onto the boundary, yielding a reduced dynamic system expressed solely in terms of boundary DOFs, as expressed by:

$$\begin{bmatrix} \boldsymbol{D}^{\mathrm{C}}_{\mathrm{LL}} & \boldsymbol{D}^{\mathrm{C}}_{\mathrm{LR}} \\ \boldsymbol{D}^{\mathrm{C}}_{\mathrm{RL}} & \boldsymbol{D}^{\mathrm{C}}_{\mathrm{RR}} \end{bmatrix} \begin{bmatrix} \boldsymbol{q}_{\mathrm{L}} \\ \boldsymbol{q}_{\mathrm{R}} \end{bmatrix} = \begin{bmatrix} \boldsymbol{f}_{\mathrm{L}} \\ \boldsymbol{f}_{\mathrm{R}} \end{bmatrix} \tag{2}$$

where the superscript C indicates the condensed dynamic stiffness matrix. Since the condensation process may involve a substantial number of DOFs, the Craig–Bampton (CB) modal synthesis method is recommended to enhance computational efficiency [43, 44].

Applying Bloch's theorem [45] along with displacement continuity and force equilibrium at the cell boundaries leads to the following expression:

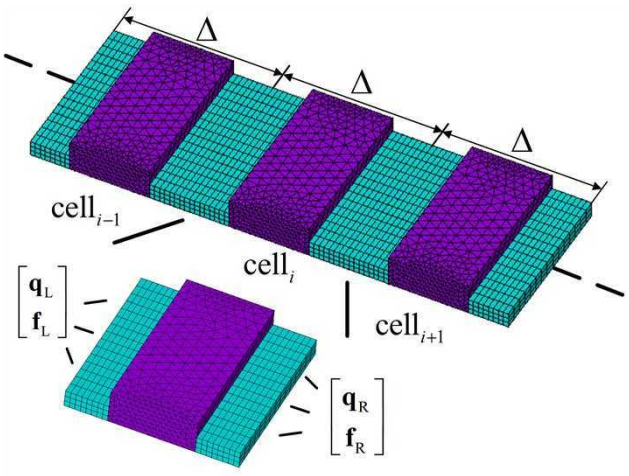

Figure 1: Schematic diagram of unit cell in periodic structure

$$\begin{bmatrix} \boldsymbol{q}_{\mathrm{R}} \\ -\boldsymbol{f}_{\mathrm{R}} \end{bmatrix} = \mu \begin{bmatrix} \boldsymbol{q}_{\mathrm{L}} \\ \boldsymbol{f}_{\mathrm{L}} \end{bmatrix} \tag{3}$$

where $\mu = e^{-jk\Delta}$ characterizes the phase shift and amplitude variation of the guided wave after traversing one unit cell; k denotes the wavenumber; Δ indicates the length of the unit cell, and $j = \sqrt{-1}$. By interchanging the displacement and force terms in Eq. 2 and incorporating Eq. 3, the eigenvalue problem of the transfer matrix is obtained, i.e.

$$(\boldsymbol{S} - \mu \boldsymbol{I}) \begin{pmatrix} \boldsymbol{q}_{\mathrm{L}} \\ \boldsymbol{f}_{\mathrm{L}} \end{pmatrix} = \boldsymbol{0} \tag{4}$$

which is commonly referred to as the transfer matrix scheme [46, 47]. The transfer matrix $\boldsymbol{S}$ writes

$$\boldsymbol{S} = \begin{bmatrix} -\left(\boldsymbol{D}^{\mathrm{C}}_{\mathrm{LR}}\right)^{-1}\boldsymbol{D}^{\mathrm{C}}_{\mathrm{LL}} & \left(\boldsymbol{D}^{\mathrm{C}}_{\mathrm{LR}}\right)^{-1} \\ -\boldsymbol{D}^{\mathrm{C}}_{\mathrm{RL}} + \boldsymbol{D}^{\mathrm{C}}_{\mathrm{RR}}\left(\boldsymbol{D}^{\mathrm{C}}_{\mathrm{LR}}\right)^{-1}\boldsymbol{D}^{\mathrm{C}}_{\mathrm{LL}} & -\boldsymbol{D}^{\mathrm{C}}_{\mathrm{RR}}\left(\boldsymbol{D}^{\mathrm{C}}_{\mathrm{LR}}\right)^{-1} \end{bmatrix} \tag{5}$$

It has been proven by Zhong and Williams that the S matrix is a symplectic matrix [25], which denotes

$$\boldsymbol{S}^{\mathrm{T}}\boldsymbol{J}_n\boldsymbol{S} = \boldsymbol{J}_n \tag{6}$$

where $\boldsymbol{J}_n$ is the symplectic identity matrix

$$\boldsymbol{J}_n = \begin{bmatrix} \mathbf{0} & \boldsymbol{I}_n \\ -\boldsymbol{I}_n & \mathbf{0} \end{bmatrix} \tag{7}$$

Since Eq. 4 defines a symplectic eigenvalue problem, its eigenvalues are known to occur in reciprocal pairs, i.e., (μ, μ^{-1}), typically associated with right- and left-going waves, respectively. When $|\mu| \neq 1$, the mode is evanescent; the root with $|\mu| > 1$ corresponds to a left-going wave, and its reciprocal, with $|\mu| < 1$, to a right-going wave. For propagating modes ($|\mu| = 1$), the direction is conventionally inferred from the sign of $\mathrm{Re}(k)$: positive values indicate right-going propagation, while negative values indicate left-going propagation.

Once the symplectic eigenvalue problem in Eq. 4 is solved, the displacement vector $\boldsymbol{q}_\mathrm{R}$ is obtained by substituting μ and $\boldsymbol{q}_\mathrm{L}$ into the first row of Eq. 3. The internal displacement vector $\boldsymbol{q}_\mathrm{I}$ is then computed via the third row of Eq. 1, thereby reconstructing the full wave field within the unit cell.

2.1.2. Mead scheme

However, computing the transfer matrix $\boldsymbol{S}$ involves inverting the dynamic stiffness matrix $\boldsymbol{D}^\mathrm{C}_\mathrm{LR}$, which is known to be numerically ill-conditioned, even when it is theoretically invertible.

From the interface equilibrium condition in Eq. 3, the force vector is expressed in terms of the displacement vector, leading to the formulation of a quadratic eigenvalue problem, as originally proposed by Mead [22, 23], i.e.

$$\left[\mu^2 \boldsymbol{D}_\mathrm{LR} + \mu\left(\boldsymbol{D}_\mathrm{LL} + \boldsymbol{D}_\mathrm{RR}\right) + \boldsymbol{D}_\mathrm{RL}\right] \boldsymbol{q}_\mathrm{L} = \mathbf{0} \tag{8}$$

Together with the displacement continuity condition in Eq.5, Eq.8 can be recast into a matrix form, leading to Mead's scheme

$$\left(\boldsymbol{N} - \mu \boldsymbol{L}\right) \begin{bmatrix} \boldsymbol{q}_\mathrm{L} \\ \boldsymbol{q}_\mathrm{R} \end{bmatrix} = \mathbf{0} \tag{9}$$

where

$$\boldsymbol{N} = \begin{bmatrix} \mathbf{0} & \boldsymbol{I} \\ -\boldsymbol{D}^\mathrm{C}_\mathrm{LR} & -\boldsymbol{D}^\mathrm{C}_\mathrm{RR} \end{bmatrix} \quad \boldsymbol{L} = \begin{bmatrix} \boldsymbol{I} & 0 \\ \boldsymbol{D}^\mathrm{C}_\mathrm{LL} & \boldsymbol{D}^\mathrm{C}_\mathrm{LR} \end{bmatrix} \tag{10}$$

This formulation can alternatively be derived from the relation $\boldsymbol{S} = \boldsymbol{N}\boldsymbol{L}^{-1}$ (see [25] for details). The main advantage of this approach is that it avoids inverting the dynamic stiffness matrix, thereby improving numerical stability.

However, it should be noted that in Eq. 10, the identity matrix and the dynamic stiffness matrix differ by several orders of magnitude. To mitigate this numerical imbalance, it is advisable to scale the identity matrix by a balancing coefficient σ. It is suggested in [28] that

$$\sigma = \frac{\left\| \boldsymbol{D}^{\mathrm{C}}_{\mathrm{RR}} \right\|_2}{n^2} \tag{11}$$

Since the eigenvectors obtained from Mead's scheme correspond to $\boldsymbol{q}_{\mathrm{L}}$ and $\boldsymbol{q}_{\mathrm{R}}$, the force component $\boldsymbol{f}_{\mathrm{L}}$ can be computed from Eq. 2 to obtain the complete eigenvector of the transfer matrix.

The Mead scheme is widely used due to its ease of implementation. However, as the number of DOFs in the unit cell increases, the eigensolution tends to include extremely large or small eigenvalues associated with strongly evanescent waves. As a result, the condition number $\mu^2_{\max}$ of the matrix increases quadratically, which may lead to numerical instability.

2.1.3. Zhong-Williams scheme

To improve the numerical conditioning, the reciprocal pairing of eigenvalues should be reformulated. Specifically, since the matrix $\boldsymbol{D}$ is real and symmetric, the following relation holds:

$$\boldsymbol{N}^{\mathrm{T}}\boldsymbol{J}\boldsymbol{N} = \boldsymbol{L}^{\mathrm{T}}\boldsymbol{J}\boldsymbol{L} = \begin{bmatrix} \boldsymbol{0} & \boldsymbol{D}^{\mathrm{C}}_{\mathrm{LR}} \\ -\boldsymbol{D}^{\mathrm{C}}_{\mathrm{RL}} & \boldsymbol{0} \end{bmatrix} \tag{12}$$

By multiplying both sides of Eq. 9 by $\boldsymbol{L}^{\mathrm{T}}\boldsymbol{J}$ and $\boldsymbol{N}^{\mathrm{T}}\boldsymbol{J}$, respectively, the following expression is obtained,

$$\boldsymbol{L}^{\mathrm{T}}\boldsymbol{J}\boldsymbol{N} \begin{bmatrix} \boldsymbol{q}_{\mathrm{L}} \\ \boldsymbol{q}_{\mathrm{R}} \end{bmatrix} = \mu \boldsymbol{L}^{\mathrm{T}}\boldsymbol{J}\boldsymbol{L} \begin{bmatrix} \boldsymbol{q}_{\mathrm{L}} \\ \boldsymbol{q}_{\mathrm{R}} \end{bmatrix} \tag{13}$$

$$\boldsymbol{N}^{\mathrm{T}}\boldsymbol{J}\boldsymbol{L} \begin{bmatrix} \boldsymbol{q}_{\mathrm{L}} \\ \boldsymbol{q}_{\mathrm{R}} \end{bmatrix} = \mu^{-1} \boldsymbol{N}^{\mathrm{T}}\boldsymbol{J}\boldsymbol{N} \begin{bmatrix} \boldsymbol{q}_{\mathrm{L}} \\ \boldsymbol{q}_{\mathrm{R}} \end{bmatrix} \tag{14}$$

By directly adding the two equations, we can obtain,

$$\boldsymbol{L}^{\mathrm{T}}\boldsymbol{J}\boldsymbol{L} \begin{bmatrix} \boldsymbol{q}_{\mathrm{L}} \\ \boldsymbol{q}_{\mathrm{R}} \end{bmatrix} = \frac{1}{\mu + \mu^{-1}} \left(\boldsymbol{L}^{\mathrm{T}}\boldsymbol{J}\boldsymbol{N} + \boldsymbol{N}^{\mathrm{T}}\boldsymbol{J}\boldsymbol{L} \right) \begin{bmatrix} \boldsymbol{q}_{\mathrm{L}} \\ \boldsymbol{q}_{\mathrm{R}} \end{bmatrix} \tag{15}$$

It can also be written in matrix form,

$$\begin{bmatrix} \mathbf{0} & \boldsymbol{D}_{\mathrm{LR}} \\ -\boldsymbol{D}_{\mathrm{RL}} & \mathbf{0} \end{bmatrix} \begin{bmatrix} \boldsymbol{q}_{\mathrm{L}} \\ \boldsymbol{q}_{\mathrm{R}} \end{bmatrix} = \lambda \begin{bmatrix} \boldsymbol{D}_{\mathrm{LR}} - \boldsymbol{D}_{\mathrm{LR}}^{\mathrm{T}} & -(\boldsymbol{D}_{\mathrm{LL}} + \boldsymbol{D}_{\mathrm{RR}}) \\ (\boldsymbol{D}_{\mathrm{LL}} + \boldsymbol{D}_{\mathrm{RR}}) & \boldsymbol{D}_{\mathrm{LR}} - \boldsymbol{D}_{\mathrm{LR}}^{\mathrm{T}} \end{bmatrix} \begin{bmatrix} \boldsymbol{q}_{\mathrm{L}} \\ \boldsymbol{q}_{\mathrm{R}} \end{bmatrix} \tag{16}$$

where

$$\lambda = \frac{1}{\mu + \mu^{-1}} \tag{17}$$

In this scheme, the generalized eigenvalue problem defined in Eq. 16 involves a skew-symmetric matrix, and is therefore classified as a generalized symplectic eigenvalue problem, as introduced by Zhong and Williams [25]. Under this transformation, the original eigenvalue pairs (μ, $1/\mu$) associated with the transfer matrix are mapped to repeated eigenvalues (λ, λ), giving rise to a double-root structure, commonly referred to as the "$S + S^{-1}$" scheme in the literature.

This scheme offers two notable advantages. First, in comparison with the Mead scheme, it yields a reduced matrix condition number of $\lambda_{\max}/2$, which helps mitigate ill-conditioning as the number of DOFs increases. Second, since the formulation is entirely constructed from the dynamic stiffness matrix, the resulting system exhibits consistent numerical scaling across its elements, potentially enhancing numerical stability.

Note that the eigenvalues are further inverted in Eq. 17, transferring them from the left-hand side to the right-hand side of the generalized eigenvalue problem in Eq. 16. As a result, the matrix subject to Householder reduction is no longer the skew-symmetric matrix on the left, which contains zero diagonal entries and may lead to numerical instability. This step is essential when using either the built-in `eig()` function or the algorithm proposed by Zhong and Williams.

An additional step is required to recover wave solutions from the generalized symplectic eigenvalue problem in Eq. 16. While the eigenvalues can be directly obtained, as shown in Eq. 17, reconstructing the eigenvectors is more involved. Previous studies [27, 29] have employed techniques such as singular value decomposition and inverse power iteration for this purpose. To bypass these procedures, we derive explicit propagation relations for wave modes within the generalized symplectic space, as detailed in the following section.

2.2. Forced Response

Once the symplectic eigensolution of the transfer matrix is obtained, the transfer function $H(\cdot)$ of the periodic structure can be constructed based on wave propagation principles, enabling direct computation of the forced response. The key idea is to express the transfer relationship of a unit cell in the wave domain. The physical displacement and force at the left boundary of adjacent unit cells are connected via the following relation:

$$\boldsymbol{S}\left[\begin{array}{c}\boldsymbol{q}_{\mathrm{p}}\\ \boldsymbol{f}_{\mathrm{p}}\end{array}\right]_{i}=\left[\begin{array}{c}\boldsymbol{q}_{\mathrm{p}}\\ \boldsymbol{f}_{\mathrm{p}}\end{array}\right]_{i+1} \tag{18}$$

where i denotes the i_{th} unit cells; the subscript p denotes the physical domain. For a given frequency, the wave basis is defined by $\lfloor\boldsymbol{\mu}\rfloor$, $\boldsymbol{\Phi}$, and $\boldsymbol{\Theta}$, where $\lfloor\boldsymbol{\mu}\rfloor$ is a diagonal matrix of μ_m, and $\boldsymbol{\Phi}$ and $\boldsymbol{\Theta}$ are the right and left eigenvector matrices of the transfer matrix. The columns of $\boldsymbol{\Phi}$ and $\boldsymbol{\Theta}$ contain the wave mode vectors $\boldsymbol{q}_{\mathrm{L}}$ and $\boldsymbol{f}_{\mathrm{L}}$. They have the following orthogonal relationship

$$\boldsymbol{\Theta}^{\mathrm{T}}\boldsymbol{S}\boldsymbol{\Phi}=\lfloor\boldsymbol{\mu}\rfloor \tag{19}$$

when eigenvectors are normalized by

$$\boldsymbol{\Phi}^{\mathrm{T}}\boldsymbol{\Theta}=\boldsymbol{I} \tag{20}$$

The physical displacement $\boldsymbol{q}_{\mathrm{p}}$ and $\boldsymbol{f}_{\mathrm{p}}$ of Eq. 18 can be represented as a linear superposition of wave modes, namely:

$$\left[\begin{array}{c}\boldsymbol{q}_{\mathrm{p}}\\ \boldsymbol{f}_{\mathrm{p}}\end{array}\right]=\left[\begin{array}{cc}\boldsymbol{\Phi}_{\mathrm{q}}^{+} & \boldsymbol{\Phi}_{\mathrm{q}}^{-}\\ \boldsymbol{\Phi}_{\mathrm{f}}^{+} & \boldsymbol{\Phi}_{\mathrm{f}}^{-}\end{array}\right]\left[\begin{array}{c}\boldsymbol{a}^{+}\\ \boldsymbol{a}^{-}\end{array}\right] \tag{21}$$

where $\boldsymbol{a}$ denotes the wave amplitudes and the superscript + and - denotes the right-going and left-going waves respectively. Substituting Eq. 19 - 21 into Eq. 18, we can obtain the propagation relation of the wave modes,

$$\boldsymbol{a}_{i+1}=\lfloor\boldsymbol{\mu}\rfloor\,\boldsymbol{a}_{i} \tag{22}$$

By applying the boundary conditions to the transfer relations, the structural transfer function can be derived. A typical periodic structure is illustrated in Fig. 2, where a force $\boldsymbol{f}_{\mathrm{e}}$ is applied at the left boundary, and a boundary condition is imposed at the right boundary. To maintain generality, the boundary condition can be expressed as follows

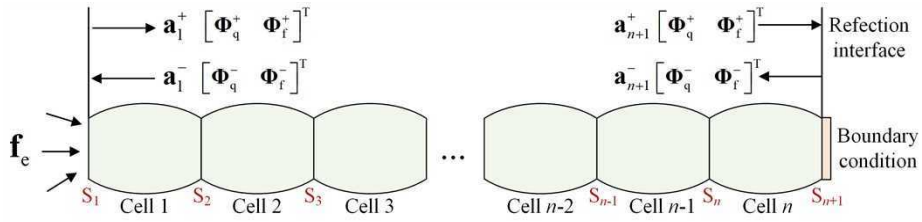

Figure 2: Wave propagation in a periodic structure with an external force applied at the left boundary and a boundary condition imposed at the right boundary

$$\boldsymbol{A}_{\mathrm{b}}\boldsymbol{f} + \boldsymbol{B}_{\mathrm{b}}\boldsymbol{q} = 0 \tag{23}$$

For fixed and free boundaries, $\boldsymbol{A}_{\mathrm{b}} = \boldsymbol{0}$, $\boldsymbol{B}_{\mathrm{b}} = \boldsymbol{I}$ and $\boldsymbol{A}_{\mathrm{b}} = \boldsymbol{I}$, $\boldsymbol{B}_{\mathrm{b}} = \boldsymbol{0}$, respectively. In the case of coupled substructures, $\boldsymbol{A}_{\mathrm{b}} = \boldsymbol{I}$ and $\boldsymbol{B}_{\mathrm{b}} = \boldsymbol{D}^{\mathrm{CS}}$, where $\boldsymbol{D}^{\mathrm{CS}}$ is the condensed dynamic stiffness matrix of the coupling element (e.g., joint or damping element). The reflection relation between right-going waves and the left-going waves writes,

$$\boldsymbol{a}_{n+1}^{-} = \boldsymbol{R}_{\mathrm{n+1}}\boldsymbol{a}_{n+1}^{+} \tag{24}$$

where

$$\boldsymbol{R}_{\mathrm{n+1}} = -\left(\boldsymbol{A}_{\mathrm{b}}\boldsymbol{\Phi}_{\mathrm{f}}^{-} + \boldsymbol{B}_{\mathrm{b}}\boldsymbol{\Phi}_{\mathrm{q}}^{-}\right)^{-1}\left(\boldsymbol{A}_{\mathrm{b}}\boldsymbol{\Phi}_{\mathrm{f}}^{+} + \boldsymbol{B}_{\mathrm{b}}\boldsymbol{\Phi}_{\mathrm{q}}^{+}\right) \tag{25}$$

Based on Eq. 22, the reflection matrix on the section 'S1' writes,

$$\boldsymbol{R}_{1} = \left\lfloor\boldsymbol{\mu}^{-}\right\rfloor^{-n}\boldsymbol{R}_{\mathrm{n+1}}\left\lfloor\boldsymbol{\mu}^{+}\right\rfloor^{n} \tag{26}$$

Furthermore, the wave amplitudes $\boldsymbol{a}_1^{+}$ and $\boldsymbol{a}_1^{-}$ can be determined by enforcing equilibrium between the total wave-induced force and the external force $\boldsymbol{f}_{\mathrm{e}}$. Once obtained, these amplitudes allow the displacement at the i_{th} section to be computed via wave propagation, namely

$$\boldsymbol{q}_i = H(i)\boldsymbol{f}_{\mathrm{e}} \tag{27}$$

where

$$H(i) = \left(\boldsymbol{\Phi}_{\mathrm{q}}^{+}\left\lfloor\boldsymbol{\mu}^{+}\right\rfloor^{i} + \boldsymbol{\Phi}_{\mathrm{q}}^{-}\left\lfloor\boldsymbol{\mu}^{-}\right\rfloor^{i}\boldsymbol{R}_{1}\right)\left(\boldsymbol{\Phi}_{\mathrm{f}}^{+} + \boldsymbol{\Phi}_{\mathrm{f}}^{-}\boldsymbol{R}_{1}\right)^{-1} \tag{28}$$

The transfer function $H(i)$ enables direct computation of the structural response to external excitation. Notably, increasing the number of periodic cells

n does not introduce additional computational complexity, as only higher powers of a diagonal matrix are required. This efficiency is a key advantage of the wave-based formulation.

Some strongly decaying wave modes are excluded from the wave basis to avoid significant numerical errors, resulting in a non-square wave mode matrix. Consequently, its pseudo-inverse needs to be computed in Eq. 25 and Eq. 28. This issue can be avoided by pre-multiplying with the left eigenvector matrix $\boldsymbol{\Theta}$. The selection of wave modes is typically based on specifying a valid range for $|\mu|$, which may vary depending on the structural model and excitation frequency. Common choices include $0.01 \leq |\mu| \leq 100$, $0.1 \leq |\mu| \leq 10$, and $0.2 \leq |\mu| \leq 5$.

2.3. power flow

Once the wave amplitudes are known, the power flow of each wave mode through the left interface of the unit cell can be computed by combining the displacement and force vectors $\boldsymbol{q}_{\mathrm{L}}$ and $\boldsymbol{f}_{\mathrm{L}}$. Although both quantities are sinusoidal, leading to oscillatory instantaneous power, the average power over a cycle can be obtained from the complex power expression:

$$\boldsymbol{p}_m = \frac{1}{2}\mathrm{Re}\left(-j\omega \boldsymbol{f}_m^{\mathrm{T}} \boldsymbol{q}_m\right) \tag{29}$$

For clarity, the subscript L indicating evaluation at the left interface of the unit cell is omitted. A positive value of p_m corresponds to energy propagation in the positive direction, while a negative value indicates propagation in the opposite direction.

Power flow provides a fundamental and quantitative basis for analyzing energy propagation in periodic structures. It enables the identification of wave modes that effectively carry energy, including certain evanescent modes not evident from μ alone. It also reveals dominant energy carriers, offering guidance for the design of vibration attenuation strategies.

2.4. Comments on current framework

The wave finite element (WFE) framework has been widely used for analyzing periodic structures. However, several challenges remain in its application to the computation of forced responses and power flow in complex engineering assemblies.

First, numerical inaccuracies can affect the orthogonality of wave modes. Current approaches rely on the biorthogonality between the left and right

wave mode matrices, $\mathbf{\Phi}$ and $\mathbf{\Theta}$, and their relationship with the transfer matrix, as described in Eqs. 19 and 20. These matrices are typically obtained using the Mead scheme, which does not guarantee strict orthogonality or complete diagonalizability. Such deviations become particularly problematic when displacement-based projection is used to extract wave amplitudes, as this process is highly sensitive to orthogonality errors.

Second, although the Zhong–Williams scheme offers improved numerical accuracy, it has yet to be fully integrated into the computation of forced responses and power flow. In practice, wave modes must first be extracted from the generalized symplectic eigenvalue problem (Eq. 16), then mapped back to the Mead framework, and finally reconstructed in wave space. This multi-step procedure increases implementation complexity and currently limits the practical adoption of the Zhong–Williams scheme.

Finally, the derivation of wave-based transfer functions remains strongly model-dependent. Despite the generality of the formulation in Section 2.2, analytical expressions must still be derived separately for each composite configuration. This process becomes especially cumbersome in the presence of multiple coupled substructures or when a single substructure interfaces with several periodic segments. A practical alternative is to compute the forced response using commercial finite element software and subsequently project the results into wave space to recover the displacement fields and power contributions of individual wave modes. While this approach circumvents the need for explicit derivation, it imposes stricter requirements on wave mode completeness and numerical stability, particularly the accuracy of modal orthogonality.

3. Power flow calculation method

This chapter develops a wave-based framework for power flow analysis with improved numerical robustness. First, the power orthogonality between wave modes is derived from symplectic orthogonality (SO) and symplectic adjoint orthogonality (SAO). This formulation is then extended to the Zhong–Williams scheme, where the transfer relationship of generalized symplectic eigenvectors is established. Finally, a block-diagonal expression for power flow is constructed by pairing wave modes based on power orthogonality, with each diagonal block corresponding to a mode group.

3.1. Power Orthogonality of Wave Modes

3.1.1. Symplectic orthogonality

Since the transfer matrix $\boldsymbol{S}$ is symplectic, the corresponding wave modes satisfy two orthogonality conditions. The first is symplectic orthogonality, which arises from the invariance of the symplectic form under the transfer transformation, as stated in Eq. 6. For two distinct eigenvalues μ_i and μ_j of $\boldsymbol{S}$, the corresponding eigenvalue equations are given by:

$$\boldsymbol{S}\boldsymbol{\phi}_i = \mu_i \boldsymbol{\phi}_i \quad \boldsymbol{S}\boldsymbol{\phi}_j = \mu_j \boldsymbol{\phi}_j \tag{30}$$

For simplicity, we use $\boldsymbol{\phi}$ to denote the eigenvector composed of $\boldsymbol{q}_{\mathrm{L}}$ and $\boldsymbol{f}_{\mathrm{L}}$. Multiplying both sides of Eq. 6 by $\boldsymbol{\phi}_i$ and $\boldsymbol{\phi}_j$, yields,

$$\boldsymbol{\phi}_i^{\mathrm{T}} \boldsymbol{S}^{\mathrm{T}} \boldsymbol{J} \boldsymbol{S} \boldsymbol{\phi}_j = \boldsymbol{\phi}_i^{\mathrm{T}} \boldsymbol{J} \boldsymbol{\phi}_j \tag{31}$$

Considering Eq. 30, the left-hand side of Eq. 31 can be expressed as:

$$\left(\mu_i \boldsymbol{\phi}_i\right)^{\mathrm{T}} \boldsymbol{J} \left(\mu_j \boldsymbol{\phi}_j\right) = \mu_i \mu_j \boldsymbol{\phi}_i^{\mathrm{T}} \boldsymbol{J} \boldsymbol{\phi}_j \tag{32}$$

Combined with the right-hand side of Eq. 31 , the SO condition can be derived as follows:

$$\left(\mu_i \mu_j - 1\right) \boldsymbol{\phi}_i^{\mathrm{T}} \boldsymbol{J} \boldsymbol{\phi}_j = 0, \quad \mu_i \neq \frac{1}{\mu_j} \tag{33}$$

This implies that if two wave modes do not form a reciprocal eigenvalue pair (i.e., $\mu_i \mu_j \neq 1$), their eigenvectors are orthogonal under the symplectic inner product defined by $\boldsymbol{J}$. This form of orthogonality differs from the conventional notion observed in real symmetric or Hermitian systems, where modal vectors are orthogonal with respect to the Euclidean inner product. Moreover, it can be rigorously shown that $\boldsymbol{\phi}_i^{\mathrm{T}} \boldsymbol{J}$ is the left eigenvector of the symplectic matrix $\boldsymbol{S}$ corresponding to the eigenvalue μ_i, i.e., $\boldsymbol{\phi}_i^{\mathrm{T}} \boldsymbol{J} \boldsymbol{S} = \mu_i \boldsymbol{\phi}_i^{\mathrm{T}} \boldsymbol{J}$. This establishes a well-defined bi-orthogonal structure between the left and right eigenvectors of $\boldsymbol{S}$, consistent with standard formulations in generalized eigenvalue theory.

While the SO holds for any symplectic matrix, its application to the transfer matrix $\boldsymbol{S}$ carries a clear physical interpretation, since the eigenvectors correspond to physical quantities. As a result, Eq. 33 can be reformulated as:

$$\left(\left(\boldsymbol{f}_{\mathrm{L}}^{j}\right)^{\mathrm{T}} \boldsymbol{q}_{\mathrm{L}}^{i} - \left(\left(\boldsymbol{f}_{\mathrm{L}}^{i}\right)^{\mathrm{T}} \boldsymbol{q}_{\mathrm{L}}^{j} \right)^{\mathrm{T}} \right) = 0 \quad \mu_i \neq \tfrac{1}{\mu_j} \tag{34}$$

This implies that the real parts of the two terms in Eq. 34 are equal, while the sum of their imaginary parts vanishes. Referring to the power expression defined in Eq. 29, multiplying Eq. 34 by $-1/2j\omega$ and taking the real part yields

$$\frac{1}{2}\ \mathrm{Re}\left(-\mathrm{j}\omega \left(\boldsymbol{f}_{\mathrm{L}}^{j}\right)^{\mathrm{T}} \boldsymbol{q}_{\mathrm{L}}^{i}\right) + \tfrac{1}{2}\mathrm{Re}\left(-\mathrm{j}\omega (\boldsymbol{f}_{\mathrm{L}}^{i})^{\mathrm{T}} \boldsymbol{q}_{\mathrm{L}}^{j}\right) = 0 \quad \mu_i \neq \tfrac{1}{\mu_j} \tag{35}$$

namely,

$$\mathrm{P}_{ij} + \mathrm{P}_{ji} = 0 \quad \mu_i \neq \tfrac{1}{\mu_j} \tag{36}$$

This result indicates that the net power exchanged between two distinct wave modes is zero, thereby imparting a clear physical meaning to SO in the context of wave propagation. In particular, it reflects the principle of power orthogonality, whereby each wave mode transports energy independently without transferring power to other modes.

3.1.2. Symplectic adjoint orthogonality

Assume that the Mead scheme yields two eigenvalues, μ_i and μ_j, with corresponding eigenvectors $\boldsymbol{\psi}_i$ and $\boldsymbol{\psi}_j$. These eigenvectors are solutions of Eq. 9 and are denoted by $\boldsymbol{\psi}$ to distinguish them from the transfer matrix eigenvectors $\boldsymbol{\phi}$. The associated eigensolutions can thus be written as:

$$\boldsymbol{N}\boldsymbol{\psi}_i = \mu_i \boldsymbol{L}\boldsymbol{\psi}_i \quad \boldsymbol{N}\boldsymbol{\psi}_j = \mu_j \boldsymbol{L}\boldsymbol{\psi}_j \tag{37}$$

By left-multiplying Eq. 12 with the eigenvector $\boldsymbol{\psi}_i^{\mathrm{T}}$ and right-multiplying it with the eigenvector $\boldsymbol{\psi}_j$, the following expression is obtained:

$$(\boldsymbol{N}\boldsymbol{\psi}_i)^{\mathrm{T}} \boldsymbol{J}\, (\boldsymbol{N}\boldsymbol{\psi}_j) = \boldsymbol{\psi}_i^{\mathrm{T}} \boldsymbol{L}^{\mathrm{T}} \boldsymbol{J}\boldsymbol{L}\boldsymbol{\psi}_j \tag{38}$$

Substituting Eq. 37 into Eq. 38 yields,

$$(1 - \mu_i\mu_j)\, \boldsymbol{\psi}_i^{\mathrm{T}} \boldsymbol{L}^{\mathrm{T}} \boldsymbol{J}\boldsymbol{L}\boldsymbol{\psi}_j = 0 \tag{39}$$

Symplectic adjoint orthogonality writes

$$\boldsymbol{\psi}_i^{\mathrm{T}} \boldsymbol{L}^{\mathrm{T}} \boldsymbol{J}\boldsymbol{L}\boldsymbol{\psi}_j = 0 \quad \mu_i \neq \tfrac{1}{\mu_j} \tag{40}$$

Similarly, we can also get

$$\boldsymbol{\psi}_i^{\mathrm{T}} \boldsymbol{N}^{\mathrm{T}} \boldsymbol{J} \boldsymbol{N} \boldsymbol{\psi}_j = 0 \quad \mu_i \neq \tfrac{1}{\mu_j} \tag{41}$$

It can be rigorously verified that both $\boldsymbol{JL\psi}$ and $\boldsymbol{JN\psi}$ serve as left eigenvectors in the Mead scheme. Accordingly, the SAO defines a bi-orthogonal structure between the right eigenvector $\boldsymbol{\psi}$ and its associated left eigenvectors, under the weighting matrices $\boldsymbol{L}$ and $\boldsymbol{N}$, respectively. Specifically, $\boldsymbol{\psi}$ is orthogonal to $\boldsymbol{JL\psi}$ with respect to $\boldsymbol{L}$, and to $\boldsymbol{JN\psi}$ with respect to $\boldsymbol{N}$.

By expressing $\boldsymbol{\psi}$ as $\left[\boldsymbol{q}_{\mathrm{L}}^{\mathrm{T}}, \boldsymbol{q}_{\mathrm{R}}^{\mathrm{T}}\right]^{\mathrm{T}}$ and substituting Eq. 12 into Eq. 40, the following relation is obtained:

$$\left(\boldsymbol{q}_{\mathrm{R}}^{j}\right)^{\mathrm{T}} \boldsymbol{D}_{\mathrm{RL}}^{\mathrm{C}} \boldsymbol{q}_{\mathrm{L}}^{i} = \left(\boldsymbol{q}_{\mathrm{L}}^{j}\right)^{\mathrm{T}} \boldsymbol{D}_{\mathrm{LR}}^{\mathrm{C}} \boldsymbol{q}_{\mathrm{R}}^{i} \quad \mu_i \neq \tfrac{1}{\mu_j} \tag{42}$$

Taking the transpose of Eq. 42 gives

$$\left(\left(\boldsymbol{q}_{\mathrm{R}}^{j}\right)^{\mathrm{T}} \boldsymbol{D}_{\mathrm{RL}}^{\mathrm{C}} \boldsymbol{q}_{\mathrm{L}}^{i}\right)^{\mathrm{T}} = \left(\boldsymbol{q}_{\mathrm{R}}^{i}\right)^{\mathrm{T}} \boldsymbol{D}_{\mathrm{RL}}^{\mathrm{C}} \boldsymbol{q}_{\mathrm{L}}^{j} \quad \mu_i \neq \tfrac{1}{\mu_j} \tag{43}$$

By adding the term $\left(\boldsymbol{q}_{\mathrm{L}}^{i}\right)^{\mathrm{T}} \boldsymbol{D}_{\mathrm{LL}}^{\mathrm{C}} \boldsymbol{q}_{\mathrm{L}}^{j}$ to both sides of Eq. 43, and noting that the left-hand side remains in transposed form, we obtain

$$\left(\left(\boldsymbol{q}_{\mathrm{L}}^{j}\right)^{\mathrm{T}} \boldsymbol{D}_{\mathrm{LL}}^{\mathrm{C}} \boldsymbol{q}_{\mathrm{L}}^{i} + \left(\boldsymbol{q}_{\mathrm{R}}^{j}\right)^{\mathrm{T}} \boldsymbol{D}_{\mathrm{RL}}^{\mathrm{C}} \boldsymbol{q}_{\mathrm{L}}^{i}\right)^{\mathrm{T}} = \left(\boldsymbol{q}_{\mathrm{L}}^{i}\right)^{\mathrm{T}} \boldsymbol{D}_{\mathrm{LL}}^{\mathrm{C}} \boldsymbol{q}_{\mathrm{L}}^{j} + \left(\boldsymbol{q}_{\mathrm{R}}^{i}\right)^{\mathrm{T}} \boldsymbol{D}_{\mathrm{RL}}^{\mathrm{C}} \boldsymbol{q}_{\mathrm{L}}^{j} \quad \mu_i \neq \tfrac{1}{\mu_j} \tag{44}$$

This equation is mathematically equivalent to the one obtained by explicitly expanding the force terms in Eq. 34. Alternatively, Eq. 36 can be derived from the SAO, which encapsulates the principle of power orthogonality.

In summary, both the SO and the SAO characterize the power orthogonality between wave modes from the perspective of wave propagation. Moreover, these formulations exhibit more consistent and robust numerical performance than the orthogonality between $\boldsymbol{\Phi}$ and $\boldsymbol{\Theta}$, as demonstrated in the subsequent application examples.

3.1.3. Extension of SAO to the Zhong–Williams Scheme

By multiplying both sides of Eq. 37 from the left by $\boldsymbol{\psi}_j^{\mathrm{T}} \boldsymbol{L}^{\mathrm{T}} \boldsymbol{J}$ and $\boldsymbol{\psi}_j^{\mathrm{T}} \boldsymbol{N}^{\mathrm{T}} \boldsymbol{J}$, respectively, we obtain

$$\boldsymbol{\psi}_j^{\mathrm{T}} \boldsymbol{L}^{\mathrm{T}} \boldsymbol{J} \boldsymbol{N} \boldsymbol{\psi}_i = 0 \quad \mu_i \neq \tfrac{1}{\mu_j} \tag{45}$$

$$\boldsymbol{\psi}_j^{\mathrm{T}} \boldsymbol{N}^{\mathrm{T}} \boldsymbol{J} \boldsymbol{L} \boldsymbol{\psi}_i = 0 \quad \mu_i \neq \tfrac{1}{\mu_j} \tag{46}$$

Summing Eqs. 45 and 46 yields

$$\boldsymbol{\psi}_j^{\mathrm{T}} \left(\boldsymbol{L}^{\mathrm{T}} \boldsymbol{J} \boldsymbol{N} + \boldsymbol{N}^{\mathrm{T}} \boldsymbol{J} \boldsymbol{L} \right) \boldsymbol{\psi}_i = 0 \quad \mu_i \neq \tfrac{1}{\mu_j} \tag{47}$$

This indicates that the eigenvectors obtained from the Mead scheme satisfy an adjoint orthogonality condition under the operator associated with the Zhong–Williams scheme (Eq. 15).

Furthermore, assuming that the two distinct double-root eigenvalues in the Zhong-Williams scheme are λ_i and λ_j, corresponding to the two pairs of eigenvalues $(\mu_i, 1/\mu_i)$ and $(\mu_j, 1/\mu_j)$ in the Mead scheme, their associated eigenvectors can be expressed as the linear superposition forms[],

$$\boldsymbol{\zeta}_{\lambda_i} = \boldsymbol{\psi}_{\mu_i} \alpha_1 + \boldsymbol{\psi}_{1/\mu_i} \alpha_2 \quad \boldsymbol{\zeta}_{\lambda_j} = \boldsymbol{\psi}_{\mu_j} \beta_1 + \boldsymbol{\psi}_{1/\mu_j} \beta_2 \tag{48}$$

The inner product between the eigenvectors $\boldsymbol{\zeta}_{\lambda_i}$ and $\boldsymbol{\zeta}_{\lambda_j}$, with respect to the eigenmatrix associated with the Zhong–Williams scheme, is expressed as follows:

$$\boldsymbol{\zeta}_{\lambda_i}^{\mathrm{T}} \left(\boldsymbol{L}^{\mathrm{T}} \boldsymbol{J} \boldsymbol{N} + \boldsymbol{N}^{\mathrm{T}} \boldsymbol{J} \boldsymbol{L} \right) \boldsymbol{\zeta}_{\lambda_j} = \left(\boldsymbol{\psi}_{\mu_i} \alpha_1 + \boldsymbol{\psi}_{1/\mu_i} \alpha_2 \right)^{\mathrm{T}} \left(\boldsymbol{L}^{\mathrm{T}} \boldsymbol{J} \boldsymbol{N} + \boldsymbol{N}^{\mathrm{T}} \boldsymbol{J} \boldsymbol{L} \right) \left(\boldsymbol{\psi}_{\mu_j} \beta_1 + \boldsymbol{\psi}_{1/\mu_j} \beta_2 \right) \tag{49}$$

$$\boldsymbol{\zeta}_{\lambda_i}^{\mathrm{T}} \boldsymbol{L}^{\mathrm{T}} \boldsymbol{J} \boldsymbol{L} \boldsymbol{\zeta}_{\lambda_j} = \left(\boldsymbol{\psi}_{\mu_i} \alpha_1 + \boldsymbol{\psi}_{1/\mu_i} \alpha_2 \right)^{\mathrm{T}} \boldsymbol{L}^{\mathrm{T}} \boldsymbol{J} \boldsymbol{L} \left(\boldsymbol{\psi}_{\mu_j} \beta_1 + \boldsymbol{\psi}_{1/\mu_j} \beta_2 \right) \tag{50}$$

From Eq. 40 and Eq. 47, it can be clearly observed that

$$\boldsymbol{\zeta}_{\lambda_i}^{\mathrm{T}} \left(\boldsymbol{L}^{\mathrm{T}} \boldsymbol{J} \boldsymbol{N} + \boldsymbol{N}^{\mathrm{T}} \boldsymbol{J} \boldsymbol{L} \right) \boldsymbol{\zeta}_{\lambda_j} = 0 \quad \lambda_i \neq \lambda_j \tag{51}$$

$$\boldsymbol{\zeta}_{\lambda_i}^{\mathrm{T}} \boldsymbol{L}^{\mathrm{T}} \boldsymbol{J} \boldsymbol{N} \boldsymbol{\zeta}_{\lambda_j} = 0 \quad \lambda_i \neq \lambda_j \tag{52}$$

In comparison to the SAO, this orthogonality structure can be referred to as the generalized symplectic adjoint orthogonality (GSAO).

3.2. Wave propagation

3.2.1. Wave propagation relationship of Mead scheme

Once the symplectic adjoint orthogonality and its generalized form are established, the wave propagation relationships for the Mead and Zhong–Williams schemes can be directly derived.

To enhance the numerical stability, the eigenvalues and their corresponding eigenvectors are arranged in reciprocal pairs, i.e., $[(\mu_1, 1/\mu_1), (\mu_2, 1/\mu_2), \ldots, (\mu_n, 1/\mu_n)]$. This convention is adopted throughout the following derivation. Under this ordering, the matrices $\Psi^{\mathrm{T}}\boldsymbol{L}^{\mathrm{T}}\boldsymbol{J}\boldsymbol{N}\Psi$ and $\Psi^{\mathrm{T}}\boldsymbol{L}^{\mathrm{T}}\boldsymbol{J}\boldsymbol{L}\Psi$ exhibit a block-diagonal structure:

$$\Psi^{\mathrm{T}}\boldsymbol{L}^{\mathrm{T}}\boldsymbol{J}\boldsymbol{N}\Psi = \lfloor \boldsymbol{\nu}_m \rfloor \quad m = 1, 2, \ldots, n \tag{53}$$

$$\Psi^{\mathrm{T}}\boldsymbol{L}^{\mathrm{T}}\boldsymbol{J}\boldsymbol{L}\Psi = \lfloor \boldsymbol{\chi}_m \rfloor \quad m = 1, 2, \ldots, n \tag{54}$$

where each diagonal block $\boldsymbol{\nu}_m$ and $\boldsymbol{\chi}_m$ is a 2×2 submatrix corresponding to a reciprocal pair.

Eq. 9 can be expressed as

$$\boldsymbol{N}\begin{bmatrix} \boldsymbol{q}_{\mathrm{L}} \\ \boldsymbol{q}_{\mathrm{R}} \end{bmatrix}_i = \boldsymbol{L}\begin{bmatrix} \boldsymbol{q}_{\mathrm{L}} \\ \boldsymbol{q}_{\mathrm{R}} \end{bmatrix}_{i+1} \tag{55}$$

Simultaneously, the displacement fields on both sides are projected onto the wave space Ψ and left-multiplied by $\Psi^{\mathrm{T}}\boldsymbol{L}^{\mathrm{T}}\boldsymbol{J}$. This yields the following relationship:

$$\left\lfloor {\boldsymbol{\chi}_m}^{-1}\boldsymbol{\nu}_m \right\rfloor \boldsymbol{a}_i = \boldsymbol{a}_{i+1} \tag{56}$$

It can be proven that Eq. 56 can be written as

$$\left\lfloor \begin{bmatrix} \mu_m & \\ & 1/\mu_m \end{bmatrix} \right\rfloor \boldsymbol{a}_i = \boldsymbol{a}_{i+1} \quad m = 1, 2, \ldots, n \tag{57}$$

It should be noted that Eq. 57 is consistent with Eq. 22, with the only difference being that the Mead scheme propagates $[\boldsymbol{q}_{\mathrm{L}}\ \boldsymbol{q}_{\mathrm{R}}]^{\mathrm{T}}$, whereas the transfer matrix scheme propagates $[\boldsymbol{q}_{\mathrm{L}}\ \boldsymbol{f}_{\mathrm{L}}]^{\mathrm{T}}$.

3.2.2. Wave propagation relationship of Zhong-Williams scheme

Following the same ordering principle, the eigenvalues and corresponding eigenvectors in the Zhong–Williams scheme are arranged as $[(\lambda_1, \lambda_1), (\lambda_2, \lambda_2), \ldots, (\lambda_n, \lambda_n)]$, which is adopted as the default ordering in the following. Under this convention, the matrices $\boldsymbol{Z}^{\mathrm{T}}(\boldsymbol{L}^{\mathrm{T}}\boldsymbol{J}\boldsymbol{N} + \boldsymbol{N}^{\mathrm{T}}\boldsymbol{J}\boldsymbol{L})\boldsymbol{Z}$ and $\boldsymbol{Z}^{\mathrm{T}}\boldsymbol{L}^{\mathrm{T}}\boldsymbol{J}\boldsymbol{L}\boldsymbol{Z}$ possess a block-diagonal structure:

$$\mathbf{Z}^{\mathrm{T}}\left(\boldsymbol{L}^{\mathrm{T}}\boldsymbol{J}\boldsymbol{N} + \boldsymbol{N}^{\mathrm{T}}\boldsymbol{J}\boldsymbol{L}\right)\mathbf{Z} = \lfloor \tau_m \rfloor \quad m = 1, 2, \ldots, n \tag{58}$$

$$\mathbf{Z}^{\mathrm{T}}\boldsymbol{L}^{\mathrm{T}}\boldsymbol{J}\boldsymbol{L}\mathbf{Z} = \lfloor \vartheta_m \rfloor \quad m = 1, 2, \ldots, n \tag{59}$$

where each diagonal block $\boldsymbol{\tau}_m$ and $\boldsymbol{\vartheta}_m$ is a 2×2 submatrix.

Eq. 15 can be rewritten as

$$\boldsymbol{L}^{\mathrm{T}}\boldsymbol{J}\boldsymbol{L}\left[\begin{array}{c} \boldsymbol{q}_{\mathrm{L}} \\ \boldsymbol{q}_{\mathrm{R}} \end{array}\right]_{i+1} = \left(\boldsymbol{L}^{\mathrm{T}}\boldsymbol{J}\boldsymbol{N} + \boldsymbol{N}^{\mathrm{T}}\boldsymbol{J}\boldsymbol{L}\right)\left[\begin{array}{c} \boldsymbol{q}_{\mathrm{L}} \\ \boldsymbol{q}_{\mathrm{R}} \end{array}\right] - \boldsymbol{L}^{\mathrm{T}}\boldsymbol{J}\boldsymbol{L}\left[\begin{array}{c} \boldsymbol{q}_{\mathrm{L}} \\ \boldsymbol{q}_{\mathrm{R}} \end{array}\right]_{i-1} \tag{60}$$

The displacement field is first projected onto the generalized symplectic basis $\boldsymbol{Z}$, and subsequently left-multiplied by $\boldsymbol{Z}^{\mathrm{T}}$. This operation, supported by the GSAO, diagonalizes the corresponding coefficient matrix into block form, namely

$$\lfloor \vartheta_m \rfloor \boldsymbol{b}_{i+1} = \lfloor \tau_m \rfloor \boldsymbol{b}_i - \lfloor \vartheta_m \rfloor \boldsymbol{b}_{i-1} \tag{61}$$

It can be proven that Eq. 61 can be written as

$$\boldsymbol{b}_{i+1} = \left\lfloor \left[\begin{array}{cc} \lambda_m & \\ & \lambda_m \end{array}\right] \right\rfloor \boldsymbol{b}_i - \boldsymbol{b}_{i-1} \quad m = 1, 2, \ldots, n \tag{62}$$

The coefficient vector $\boldsymbol{b}$ consists of n block pairs, $[(b_{11}, b_{12}), (b_{21}, b_{22}), \ldots, (b_{n1}, b_{n2})]$, each associated with a distinct eigensubspace. Although the eigenvectors corresponding to λ_m in the Zhong–Williams scheme do not directly represent wave modes, they span the same subspace as the mode vectors associated with μ_m and $1/\mu_m$ in the Mead scheme. Consequently, each pair (b_{m1}, b_{m2}) represents the projection of the displacement field onto the corresponding modal subspace. Within this framework, the vector $\boldsymbol{b}$ can be interpreted as a generalized wave amplitude.

The wave propagation relationship established in Eq. 62 can be directly embedded into the existing wave finite element framework, enabling the

Zhong–Williams scheme to independently compute wave propagation, forced response, and power flow. For the sake of clarity, the detailed derivation of the transfer function $H^{\mathrm{Z}}(\cdot)$, based on the Zhong–Williams scheme, is provided in Appendix A.

It should be noted that in certain symmetric structures such as cylinders exhibiting repeated-root wave modes, the computational formulation remains unchanged; however, the corresponding cell-block elements increase in size to 4×4.

3.3. power flow based on power orthogonality

Expanding the boundary displacement and force in terms of wave modes, The total power flow through the boundary section is then given by:

$$P_{\mathrm{total}} = \mathrm{Re}\left(-j\omega\frac{1}{2}\boldsymbol{f}^{\mathrm{T}}\boldsymbol{q}\right) = \frac{1}{2}\mathrm{Re}\left(-j\omega\sum_{i=1}^{n}\sum_{j=1}^{n}\left(a_i\boldsymbol{f}_{\mathrm{L}}^{i}\right)^{\mathrm{T}}a_j\boldsymbol{q}_{\mathrm{L}}^{j}\right) \tag{63}$$

Based on the power orthogonality given in Eq. 35, the net power exchange between unpaired wave modes vanishes. Accordingly, Eq. 63 simplifies to:

$$P_{\mathrm{total}} = \frac{1}{2}\mathrm{Re}\left(-j\omega\left(\sum_{i=1}^{n/2}\left(\left(a_{i,1}\boldsymbol{f}_{\mathrm{L}}^{i,1}+a_{i,2}\boldsymbol{f}_{\mathrm{L}}^{i,2}\right)^{\mathrm{T}}\left(a_{i,1}\boldsymbol{q}_{\mathrm{L}}^{i,1}+a_{i,2}\boldsymbol{q}_{\mathrm{L}}^{i,2}\right)\right)\right)\right) \tag{64}$$

Here, the pairs $(\boldsymbol{q}_{\mathrm{L}}^{i,1}, \boldsymbol{f}_{\mathrm{L}}^{i,1})$ and $(\boldsymbol{q}_{\mathrm{L}}^{i,2}, \boldsymbol{f}_{\mathrm{L}}^{i,2})$ correspond to wave modes with eigenvalues (μ, μ^{-1}) or (λ, λ). For double-root wave modes, the expansion in Eq. 64 additionally includes $(\boldsymbol{q}_{\mathrm{L}}^{i,3}, \boldsymbol{f}_{\mathrm{L}}^{i,3})$ and $(\boldsymbol{q}_{\mathrm{L}}^{i,4}, \boldsymbol{f}_{\mathrm{L}}^{i,4})$.

As shown in Eq. 64, power interaction may occur between paired wave mode. Computing the power contribution of individual modes may underestimate the total power. Therefore, in the following analysis, the power associated with each wave mode pair is evaluated collectively.

4. Numerical validation

4.1. simulated model

The proposed formulation is verified using representative models composed of fundamental structural components: beams and cylindrical shells.

The corresponding finite element models are shown in Fig. 3(a) and Fig. 3(b). All simulations employ `SOLID185` elements with steel as the material, characterized by $E = 2 \times 10^{11}$ Pa, $\nu = 0.3$, and $\rho = 7.8 \times 10^3$ kg/m^3.

The beam unit cell measures 30 mm in length, 60 mm in width, and 10 mm in height. The cylindrical shell unit cell has a radius of 200 mm, a thickness of 5 mm, and an axial length of 200 mm. To simulate the forced response, the unit cell is axially repeated ten times. A harmonic force is applied at one end, with the other end left free. The cross-section denoted by 'S' is used to extract displacement and power flow for evaluation.

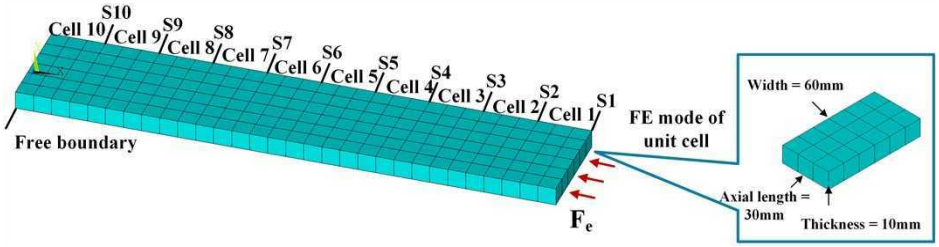

(a)

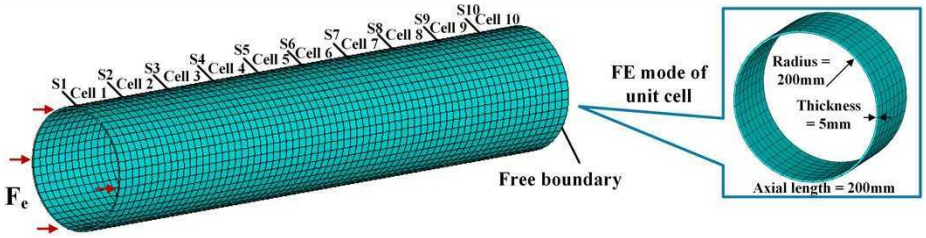

(b)

Figure 3: Finite element models for unit cells and forced response analysis: (a) beam and (b) cylindrical shell, where 'S' denotes section, one boundary is subjected to a force load, and the opposite boundary is free.

Figure 4 shows the dispersion curves for the beam and cylindrical shell, computed over the frequency range 0–5000 Hz using both the Mead and Zhong–Williams schemes. The results from the two formulations are in good agreement. Each wave mode can be identified by its corresponding wave shape, which, in all cases presented here, is derived from the eigenvectors of the Mead scheme. The eigenvectors from the Zhong–Williams scheme are not displayed, as they lack direct physical interpretability and may lead to ambiguity.

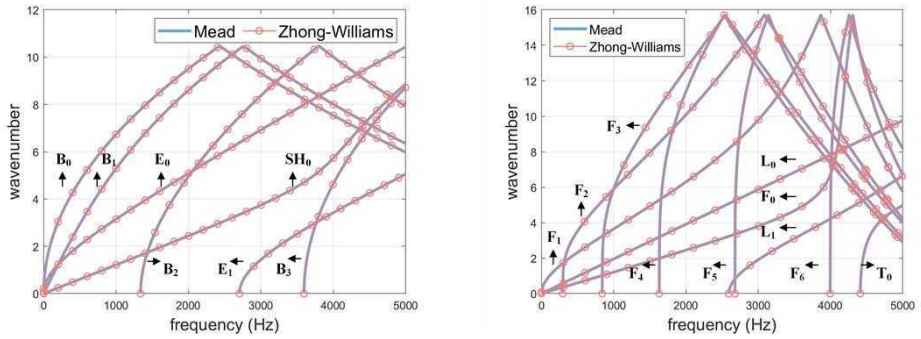

(a) (b)

Figure 4: Dispersion curves of (a) a beam and (b) a cylindrical shell. In (a), B denotes the bending wave, E the extensional wave, and SH the shear wave. In (b), F denotes the flexural wave, L the longitudinal wave, and T the torsional wave. Subscripts indicate the modal order.

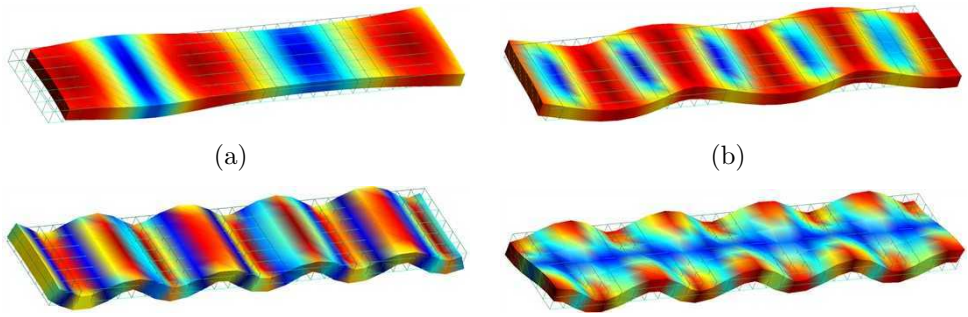

(a) (b)

(c) (d)

Figure 5: Guided wave modes in beams include: (a) the extensional mode E_0, (b) the shear horizontal mode SH_0, (c) the fundamental bending mode B_0, and (d) the first-order bending mode B_1. The subscript denotes the modal order, where 0 indicates uniform deformation across the beam width, and 1 corresponds to a deformation pattern with half a sine wave cycle.

Figure 4(a) demonstrates that the guided waves propagating in the beam include extensional, shear, and bending modes. Representative wave shapes for each type are shown in Figs. 5(a) to 5(c). The modal order can be further distinguished by examining the deformation pattern along the width direction, as illustrated in Figs. 5(c) and 5(d). A uniform widthwise deformation corresponds to the zeroth-order bending mode (B_0), whereas a half-sine distribution corresponds to the first-order mode (B_1).

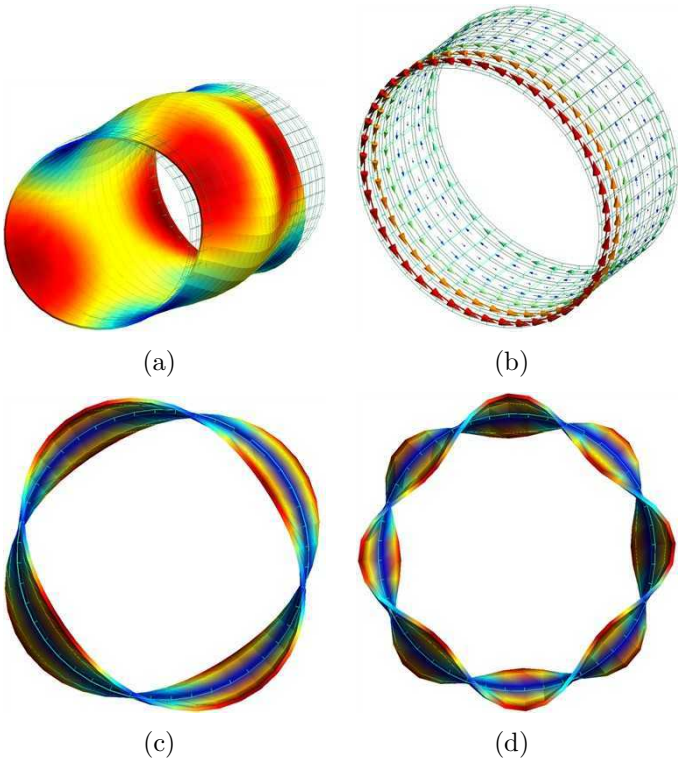

Figure 6: Guided wave modes in a cylindrical shell: (a) the longitudinal mode L_0, (b) the torsional mode T_0, (c) the second-order flexural mode F_2, and (d) the fourth-order flexural mode F_4. The subscript denotes the modal order, which corresponds to the wave numbers along the circumferential direction of the shell.

As shown in Fig. 4(b), the guided waves in the cylindrical shell include longitudinal, torsional, and flexural modes. Representative wave shapes are depicted in Figs. 6(a) to 6(d). The modal order is further classified based on the circumferential wavenumber, as illustrated in Figs. 6(c) and 6(d), corresponding to modes F_2 and F_4, respectively.

4.2. Demonstration of orthogonality

The eigenvectors corresponding to left- and right-going waves at 5000 Hz are extracted for both the beam and the cylindrical shell. These include $(\boldsymbol{\phi}_{\mathrm{q}}^{\mathrm{L}}, \boldsymbol{\phi}_{\mathrm{f}}^{\mathrm{L}})$, $(\boldsymbol{\psi}_{\mathrm{q}}^{\mathrm{L}}, \boldsymbol{\psi}_{\mathrm{q}}^{\mathrm{R}})$, and $(\boldsymbol{\zeta}_{\mathrm{q}}^{\mathrm{L}}, \boldsymbol{\zeta}_{\mathrm{q}}^{\mathrm{R}})$, representing the transfer matrix, Mead, and Zhong–Williams schemes, respectively. The eigenvectors are arranged following the ordering introduced in Sec. 3.2.

The orthogonality between left and right eigenvectors is evaluated using Eq. 20, and the resulting matrices are shown in Figs. 7(a) and 7(b) for the beam and the cylindrical shell, respectively. Significant off-diagonal values are observed, indicating deviations from ideal orthogonality. This arises because the eigenvectors of the transfer matrix are not directly computed but reconstructed via transformation from the Mead scheme, which does not numerically preserve orthogonality. Such inaccuracies may impact applications requiring strict modal orthogonality, such as wave-space projection of displacement fields.

Secondly, the SO is evaluated using Eq. 33, with the resulting matrices shown in Figs. 7(c) and 7(d). As evident from the results, only diagonal elements exhibit significant values, indicating good numerical stability of the SO. A clear block-diagonal structure is observed in Fig. 7(d): for single-root modes such as L_0, L_1, and T_0, 2×2 blocks appear; for double-root modes F_0–F_6, the corresponding blocks expand to 4×4.

Subsequently, the SAO, defined in Eq. 40, is evaluated, with the resulting matrices shown in Figs. 7(e) and 7(f). The results are identical to those in Figs. 7(c) and 7(d), confirming that the SO and SAO represent the same physical principle—power orthogonality. For consistency, the SAO is adopted in the following analyses. It is also noted that Eqs. 41, 45, and 46 are mathematically equivalent to Eq. 40, and yield identical results.

Finally, the GSAO in the Zhong–Williams scheme is verified using Eq. 51. The resulting matrices for the beam and cylindrical shell are shown in Figs. 8(a) and 8(b), respectively. Non-zero entries appear only along the diagonal, confirming that the generalized symplectic eigenvectors satisfy the GSAO. This

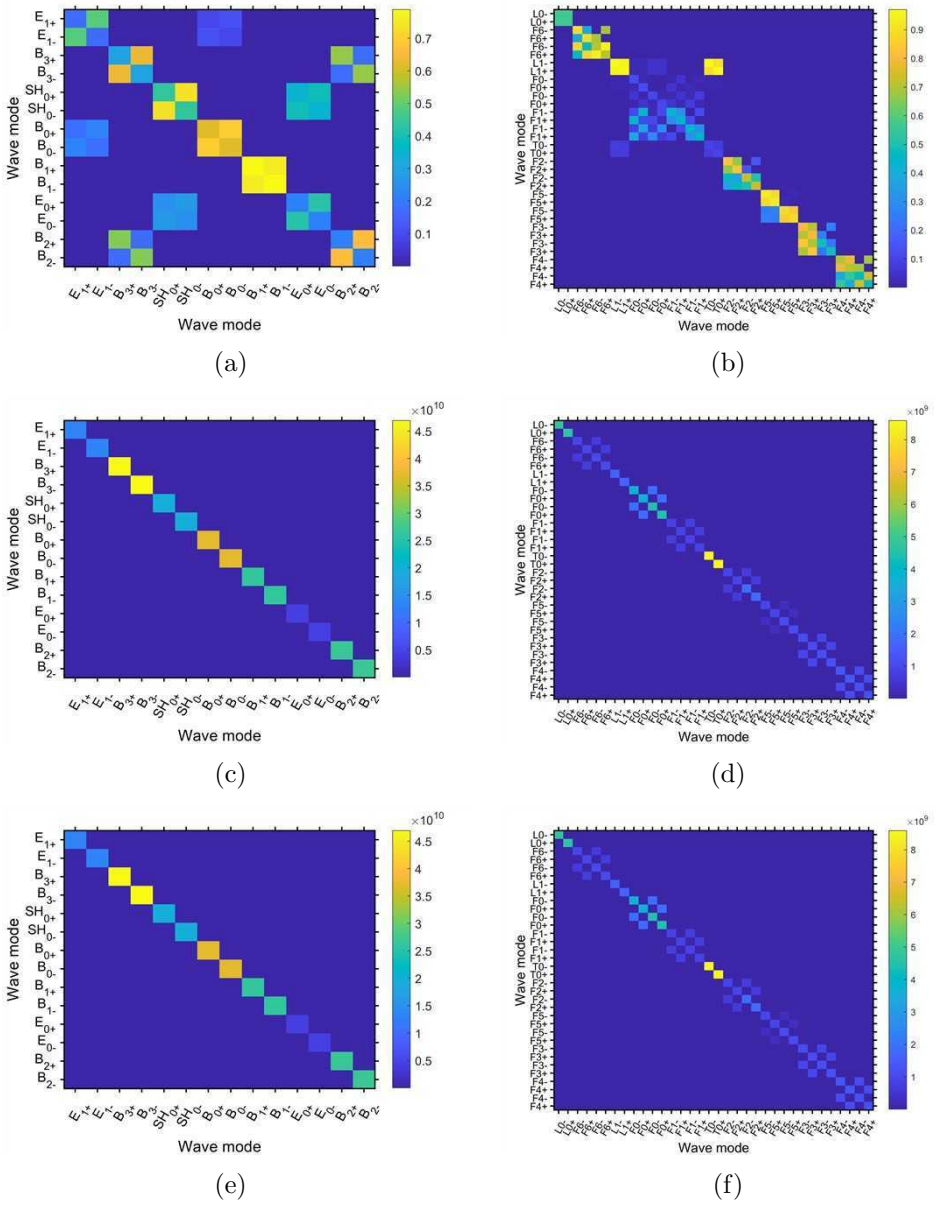

Figure 7: Orthogonalities among wave mode vectors. Both the horizontal and vertical axes represent wave modes. The matrix elements are computed using orthogonality equations. Subfigures (a) and (b) correspond to Eq. 20, (c) and (d) to Eq. 33 (SO), and (e) and (f) to Eq. 40 (symplectic adjoint orthogonality). Subfigures (a), (c), and (e) correspond to beam structures, while (b), (d), and (f) correspond to cylindrical shells.

ensures the block-diagonalization in Eqs. 58 and 59, and establishes a numerically stable propagation relation in the generalized symplectic eigenspace, as expressed in Eq. 62. It is also noted that Eq. 52 yields identical results to Eq. 51, and is therefore omitted for brevity. For better visualization, the matrix in Fig. 8(b) is plotted on a logarithmic scale in Fig. 8(c). Distinct 2×2 and 4×4 block structures are clearly observed along the diagonal.

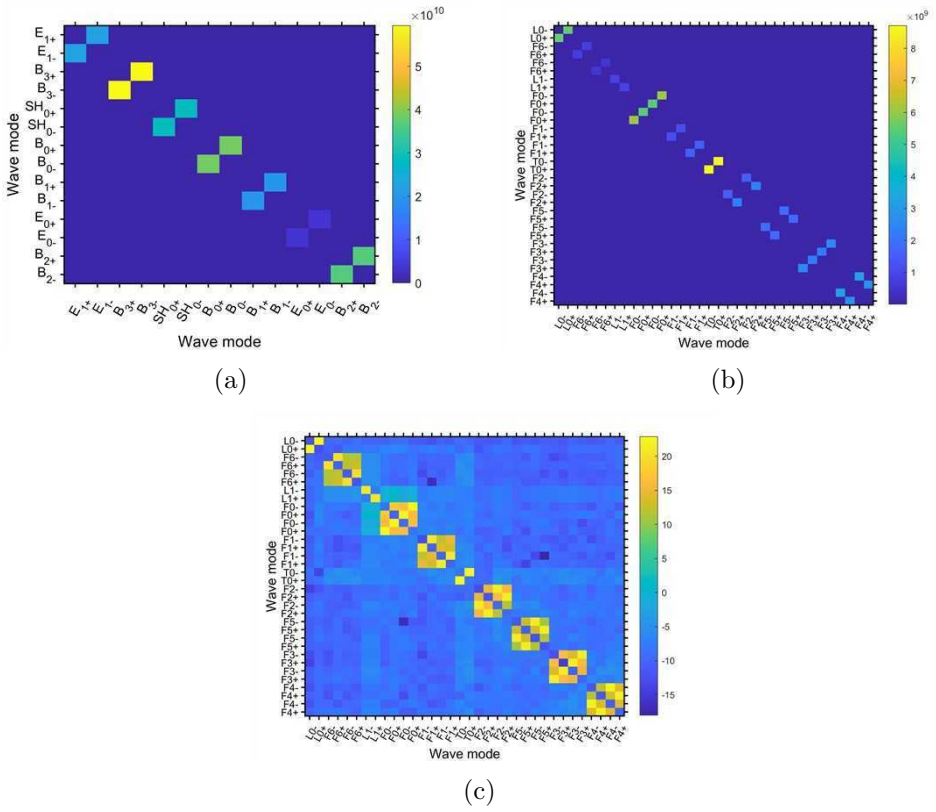

Figure 8: Generalized symplectic adjoint orthogonality. The matrix elements are computed using Eq. 51. Subfigure (a) correspond to the beam, while (b) correspond to cylindrical shells. Subfigure (c) presents the logarithmic transformation of the matrix in (b).

Furthermore, Eqs. 33–36 and 42–44 theoretically establish that both symplectic orthogonality and its adjoint form imply power orthogonality. To support this conclusion, an intuitive verification is provided. Figure 9(a) presents the power matrix $\boldsymbol{P}$, computed using Eq. 29, where each element denotes the power interaction between $\boldsymbol{f}_i$ and $\boldsymbol{q}_j$. According to Eq. 36, $\boldsymbol{P}$ is expected to exhibit a block skew-symmetric structure. To verify this, the

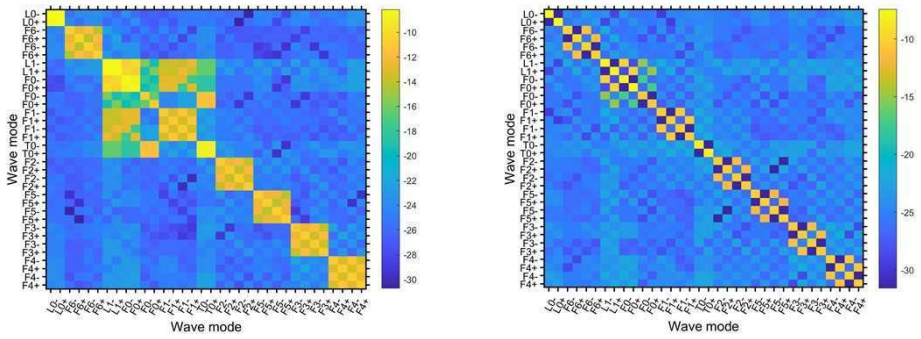

(a) (b)

Figure 9: Illustration of power orthogonality between wave modes. (a) The power matrix $\boldsymbol{P}$ is computed using Eq. 29. To exhibit the block skew-symmetric structure of the power matrix, (b) the sum $\boldsymbol{P} + \boldsymbol{P}^{\mathrm{T}}$ is evaluated. To clearly reveal the block structure, the logarithm of the matrix elements is taken.

summation $\boldsymbol{P} + \boldsymbol{P}^{\mathrm{T}}$ is calculated and shown in Fig. 9(b). The result reveals that nonzero values are strictly confined to the diagonal blocks, consistent with the theoretical prediction. This confirms the validity of Eq. 36 and thereby substantiates the power orthogonality. It is worth noting that the total power should be evaluated in block form as defined by Eq. 64; otherwise, off-diagonal elements—particularly those within repeated-root blocks—may contribute residual terms and lead to an underestimation of the total power.

4.3. forced response using Zhong-Williams scheme

A harmonic force of 100 N amplitude is applied in the x-direction at a frequency of 5000 Hz, as shown in Fig. 3. The corresponding displacement responses are computed using three approaches: the finite element method (FEM), the Mead scheme, and the Zhong–Williams scheme. Displacements in the x-direction at the S5 and S10 sections of both the beam and the cylindrical shell are extracted and plotted in Fig. 10. Overall, the results obtained from the three methods exhibit strong agreement. Minor discrepancies are observed only at certain frequency points with extremely low response amplitudes—for instance, 3800 Hz in Fig. 10(b), 4250 Hz and 4600 Hz in Fig. 10(c), and 4300 Hz in Fig. 10(d).

The forced response can be independently computed using the Zhong–Williams scheme by incorporating the transfer relation (Eq. 62), the generalized symplectic eigenvalues $\lfloor \lambda_m \rfloor$, and the corresponding eigenvectors $\boldsymbol{Z}$. The results

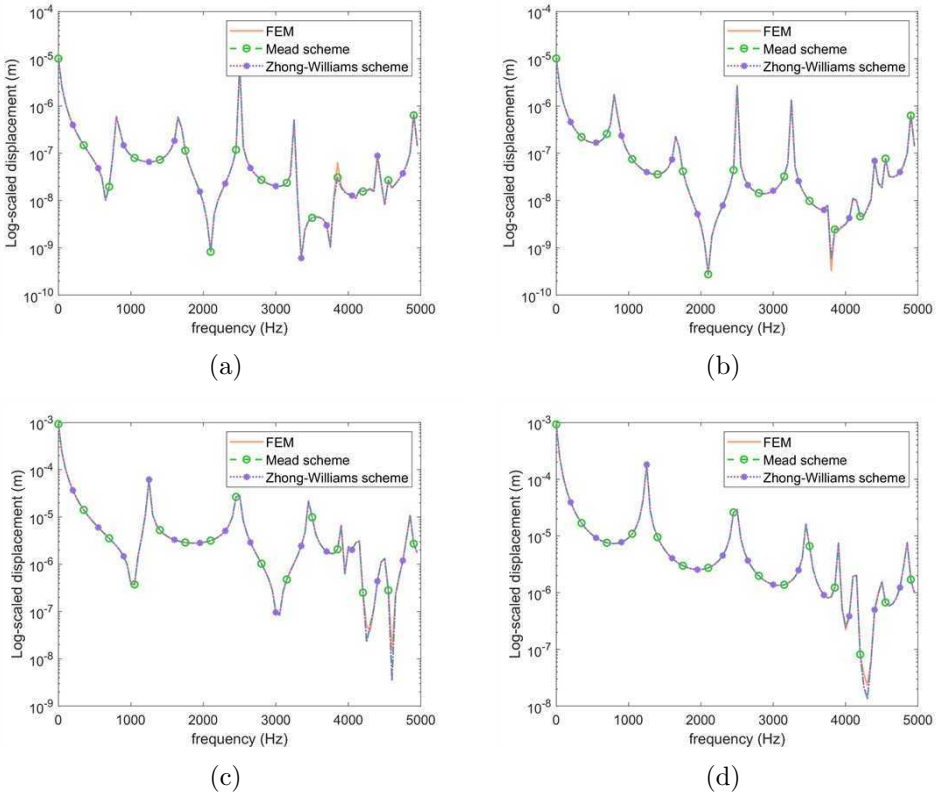

Figure 10: The x-direction displacement responses at Section 5 (a and c) and Section 10 (b and d) are computed using the finite element method, the Mead scheme, and the Zhong-Williams scheme. (a) and (b) correspond to the beam model shown in Fig. 3(a), while Figures (c) and (d) correspond to the cylindrical shell model shown in Fig. 3(b).

demonstrate numerical accuracy comparable to that of the Mead scheme for both beam and cylindrical shell structures. This approach, on the one hand, avoids the need to project the eigenvectors $\boldsymbol{Z}$ from the Zhong–Williams scheme back into the wave space, as required in previous studies [][ref]. On the other hand, it verifies the accuracy of the transfer relation defined by Eq. 62, thereby ensuring the correct computation of the generalized wave amplitude $\boldsymbol{b}$.

4.3.1. forced response using wave decomposition

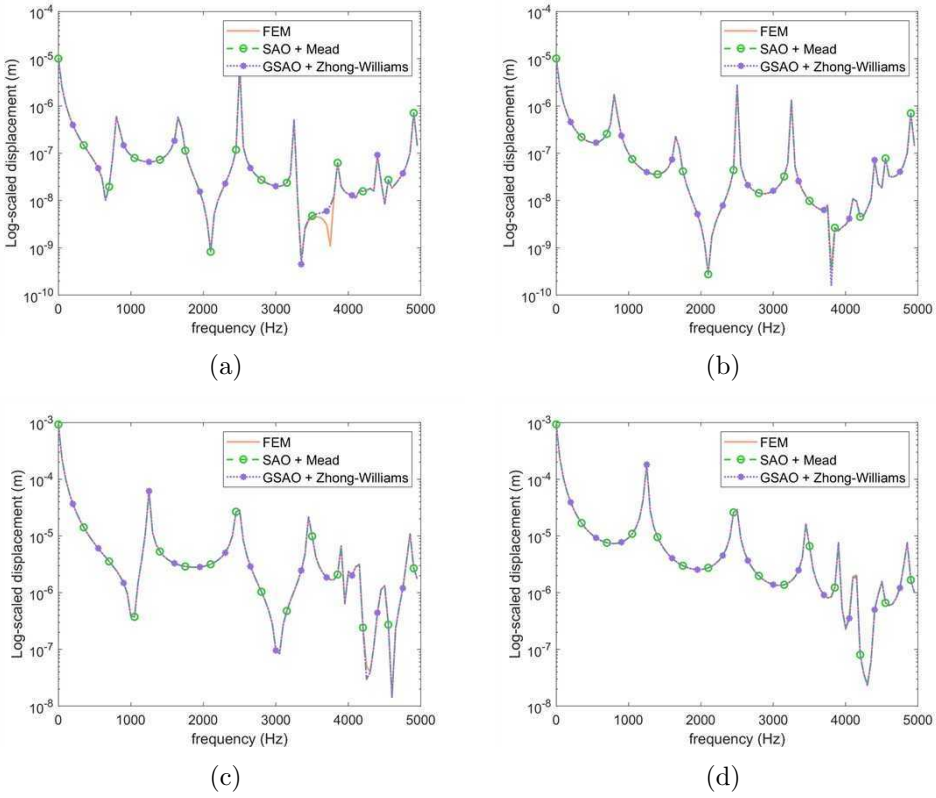

Figure 11: Reconstructed x-direction displacement responses at Section 5 (a and c) and Section 10 (b and d). (a) and (b) correspond to the beam model shown in Fig. 3(a), while Figures (c) and (d) correspond to the cylindrical shell model shown in Fig. 3(b). SAO and GSAO are employed for wave decomposition, while the Mead and Zhong-Williams schemes are utilized for wave propagation.

The wave propagation method is well-suited for periodic structures, but

becomes impractical for complex assembled structures commonly encountered in engineering practice. In such cases, commercial finite element software offers an efficient alternative for computing natural modes and forced responses. The resulting displacement fields can then be decomposed onto the wave space to evaluate the associated modal power flow.

To assess the numerical accuracy of the wave decomposition, the following procedure is employed. Based on the forced response computed by the finite element method in Sec. 4.3, the displacement of Cell 1 is first projected into the wave space using the SAO and GSAO. Specifically, two types of wave decompositions are considered:

$$\begin{bmatrix} \mathbf{q}_{\mathrm{L}} \\ \mathbf{q}_{\mathrm{R}} \end{bmatrix} = \Psi \boldsymbol{a} \quad \text{and} \quad \begin{bmatrix} \mathbf{q}_{\mathrm{L}} \\ \mathbf{q}_{\mathrm{R}} \end{bmatrix} = \mathrm{Z}\boldsymbol{b} \tag{65}$$

The modal amplitudes $\boldsymbol{a}$ and generalized amplitudes $\boldsymbol{b}$ are obtained by left-multiplying Eq. (65) with $\psi_i^{\mathrm{T}}\boldsymbol{L}^{\mathrm{T}}\boldsymbol{J}\boldsymbol{L}$ (Eq. 40) and $\boldsymbol{Z}^{\mathrm{T}}\boldsymbol{L}^{\mathrm{T}}\boldsymbol{J}\boldsymbol{L}$ (Eq. 52), respectively. The reconstructed forced responses at Sections 5 and 10 are then obtained using the propagation relations defined by the Mead and Zhong–Williams schemes, namely Eq. 57 and Eq. 62.

The results are presented in Fig. 11. It is observed that both the "SAO + Mead" and "GSAO + Zhong–Williams" schemes accurately compute the forced responses at Sections 5 and 10. This indicates that both SAO and GSAO accurately compute wave amplitudes, enabling further calculation of power flow.

4.4. power flow

Four approaches for computing power flow are summarized in Table 1. The first two determine wave amplitudes based on wave propagation and boundary conditions, suitable for periodic structures. The third and fourth utilize commercial finite element software to obtain the structural response, which is then decomposed using symplectic adjoint orthogonality (SAO) and its generalized form (GSAO) to extract the wave amplitudes. These methods are thus applicable to assembled or non-periodic structures. In all cases, the power flow is computed using Eq. 64 once the wave amplitudes are obtained.

To verify the accuracy of the proposed power calculation methods, the input and damping power obtained from finite element analysis are compared with the wave power at each section computed using all four methods. The simulation models in Fig. 3 are modified by introducing 0.1% material damping in Cell 10. For the beam, Force Load 1 applies a 100 N uniformly

Table 1: Four approaches to compute power flow

Methods	**Scheme**	**Orthogonality**	**wave amplitude computation**	**applicable structure**
M1	Mead	SAO	wave propagation + boundary condition	periodic
M2	ZW	GSAO	wave propagation + boundary condition	periodic
M3	Mead	SAO	FEM + Wave decomposition	assembled
M4	ZW	GSAO	FEM + Wave decomposition	assembled

distributed load in the Y-direction, while Force Load 2 applies the same magnitude in the X-, Y-, and Z-directions. For the cylindrical shell, Force Load 3 is applied in the X-direction, and Force Load 4 in the X-, Y-, and Z-directions, each with a magnitude of 100 N.

The average damping power over one cycle is given by

$$p_{\text{damp}} = \frac{1}{2}\omega^2 \,\text{Re}\left(\boldsymbol{q}_c^{\text{T}} \boldsymbol{C} \boldsymbol{q}_c\right), \tag{66}$$

where $\boldsymbol{C}$ is the damping matrix of Cell 10, and $\boldsymbol{q}_c$ denotes its displacement response. Damping power is typically negative, indicating energy dissipation, while external force power is generally positive, representing energy input. The sign of wave mode power reflects the direction of energy transmission across the section: positive values indicate propagation in the positive direction, and negative values indicate propagation in the negative direction.

The results are shown in Fig. 12, where subfigures (a) and (b) illustrate the power flow in the beam under Force Load 1 and Force Load 2, respectively, and subfigures (c) and (d) depict the power flow in the cylindrical shell under Force Load 3 and Force Load 4. The input power, damping power, and total transmitted power computed by Methods M1–M4 across sections S1 to S9 (excluding S3–S8 for clarity) show excellent agreement. This consistency confirms the accuracy of the proposed power flow calculation methods.

Furthermore, the power flow reveals richer information about the struc-

tural vibration behavior. In Fig. 12(a), the Y-direction force primarily excites mode B0, with minor excitation of mode B3. In Fig. 12(b), the additional application of forces in the X- and Z-directions leads to the excitation of modes E0 and SH0. Notably, the power carried by SH0 propagates in the negative direction, partially offsetting the net positive power transmission. In Fig. 12(c), the X-direction force exclusively excites mode E0. When forces are applied in both the X- and Z-directions, the power associated with the excited mode F1 becomes significantly larger than that of modes L0 and F0.

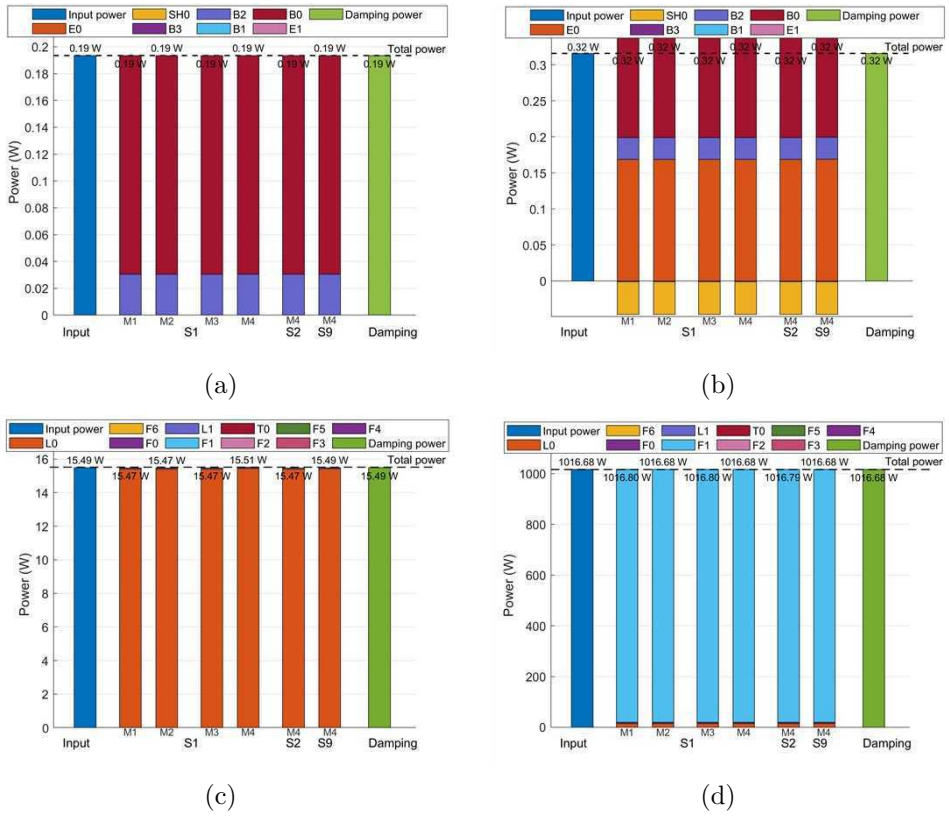

Figure 12: Power flow of beam (a)(b) and cylindrical shell (c)(d) under force load: (a) a 100 N load uniformly distributed along the Y-direction, (b) a 100 N load uniformly distributed along the X-, Y-, and Z-directions, (c) a 100 N load uniformly distributed along the X-direction, (d) a 100 N load uniformly distributed along the X-, Y-, and Z-directions. The 0.1% material damping is introduced in Cell 10 of FE model in Fig. 3.

5. Application: Power Flow in Electric Motor Housing

Effective vibration control requires a clear understanding of energy transmission in assembled structures with multiple propagation paths, such as the motor housing assembly. As shown in Fig. 13, the FE model denotes a simplified version of the electric motor housing. The motor is mounted on a structural support, with a damping pad inserted in between to dissipate vibration energy. The motor shaft extends toward the rear of the shell and is supported by a bearing located at its trailing end.

The primary vibration source is the unbalanced force of the shaft. Therefore, a total distributed load of 1000 N is applied at the axial center of the shaft, i.e., between sections S4 and S5. Given that high-speed motors typically operate at rotational speeds exceeding 10,000 rpm, the excitation frequency is set to 200 Hz. The model is constructed using SOLID185 elements with structural steel as the base material, and a material damping ratio of 0.1% is assigned to the damping pad.

The analysis employs Method 4 in Tab. 1, which combines commercial FE analysis for forced response, the Zhong–Williams scheme for wave-mode computation, and GSAO for wave decomposition. Observation sections S1–S9, as listed in Tab. 2, are used to evaluate the wave-mode power flow across the structure.

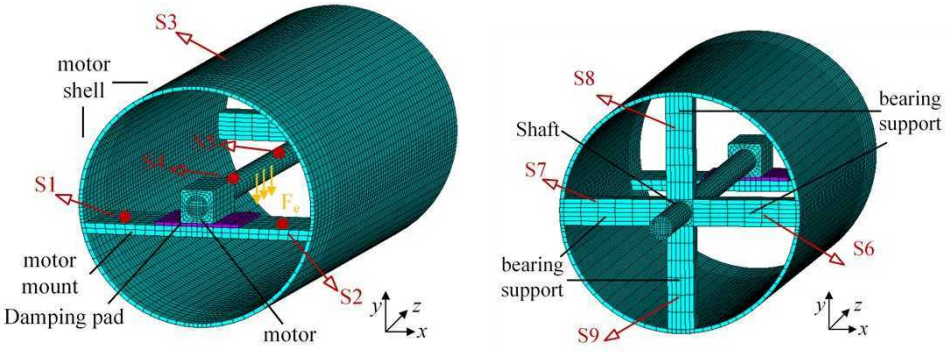

(a) (b)

Figure 13: Simplified finite element model of the lectric motor housing, including the motor, mount, damping pad, shaft, bearing support, and shell. An external force is applied to the central segment of the shaft between sections S4 and S5. Sections S1–S9 are used to observe wave-mode energy flow.

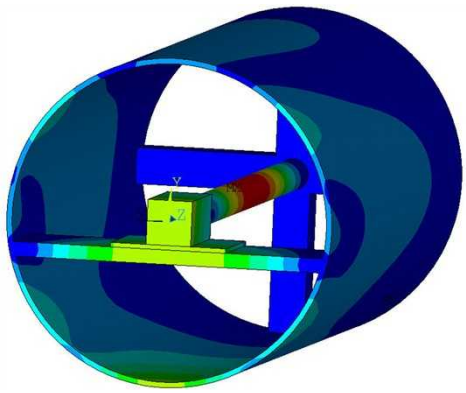

Figure 14: Forced response of electric motor housing calculated using commercial FE software.

Table 2: Observation section and its represented substructure

S1	S2	S3	S4	S5	S6	S7	S8	S9
motor mount (left)	motor mount (right)	motor shell	shaft (front)	shaft (back)	bear support (right)	bear support (left)	bear support (up)	bear support (down)

The forced response computed by the FE method is presented in Fig. 14. The corresponding power flow network is shown in Fig. 15(a), while Fig. 15(b) illustrates the wave shapes of each substructure. Here, X, Y, and Z denote bending modes along the x-, y-, and z-axes, respectively.

The power flow network reveals two distinct energy transmission paths: IP–S4–DP and IP–S5–(S6, S7, S8, S9)–S3–(S1, S2)–DP, where IP denotes the input power and DP the dissipated power due to damping. The first path serves as the primary route, with 118.32 W of power dissipated directly via section S4, accounting for 95.6% of the total input. This energy is primarily transmitted through wave modes BX (55.9 W) and BY (62.9 W), indicating that implementing damping treatment at the motor mount can effectively suppress structural vibration.

Although this path accounts for only 5.38 W (4.4%) of the transmitted power, it serves as the primary contributor to shell-borne noise. We can observe two features from the power flow network. First, the dominant wave modes within the shell are modes T0 and F2. If a bandgap-based noise reduction strategy is considered, these modes should be treated as primary

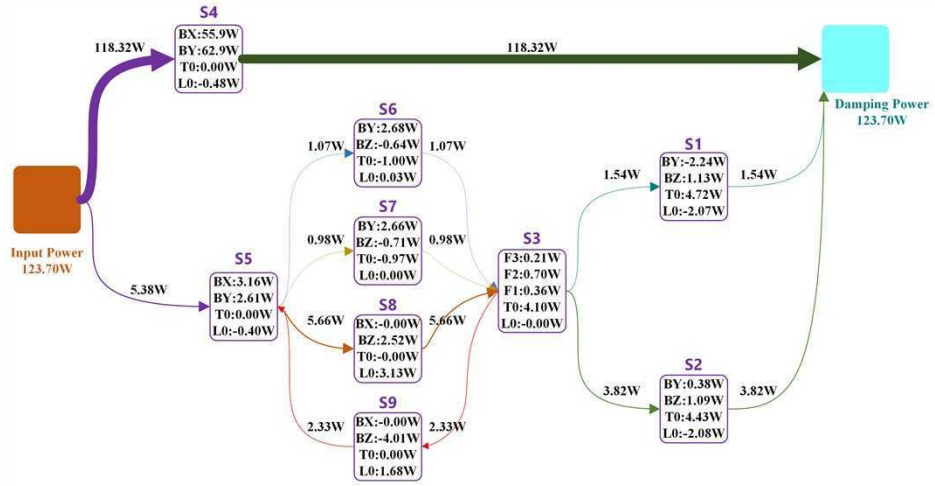

(a)

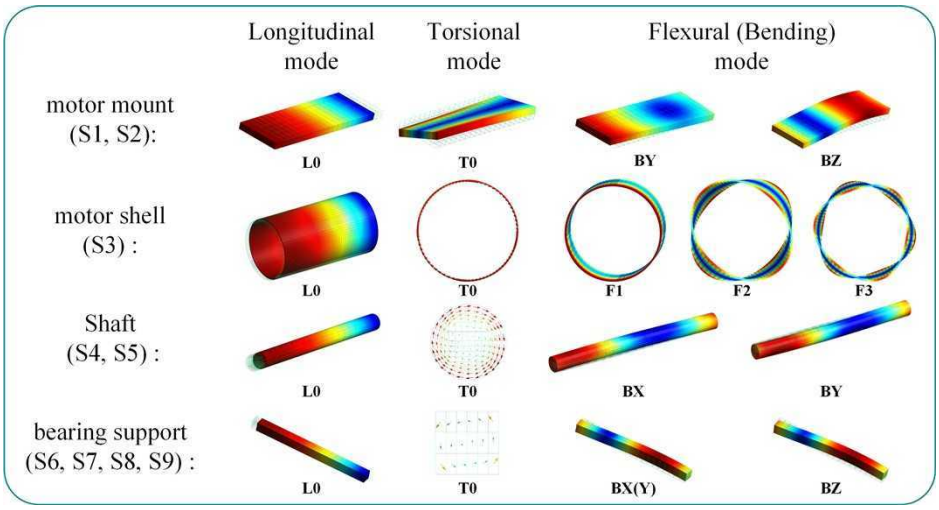

(b)

Figure 15: (a) Power flow network of the electric motor housing under the forced response shown in Fig. 14, obtained using Method M4; (b) wave shapes involved in the power flow network.

targets. Second, the power flow at section S9 is oriented oppositely to that at sections S6, S7, and S8, with mode BZ alone transmitting up to 4.01 W. This suggests the presence of a localized energy circulation, implying that damping applied at S9 could simultaneously attenuate energy transmission through S6–S8.

6. conclusion

This study proposes a power flow calculation method based on guided waves within the framework of the Zhong–Williams scheme. The method is validated through numerical simulations of both forced response and power flow on beam and cylindrical shell structures, and further applied to construct the wave-mode power flow network of an electric motor housing.

Power orthogonality, derived from the symplectic orthogonality, offers numerical stability and enables accurate wave propagation and decomposition. Building on this, its extension to the Zhong–Williams scheme yields the generalized symplectic adjoint orthogonality, which enables diagonalization of the coefficient matrix and facilitates the derivation of the transfer relation between symplectic eigenvectors of adjacent cells. These developments allow the Zhong–Williams scheme to independently compute forced response and power flow, with results on beam and shell structures showing excellent agreement with finite element analysis.

Four power flow calculation methods are reviewed and numerically shown to yield consistent results. Based on this verification, a combined FEM and Zhong–Williams scheme is employed to construct the wave-modal power flow network of an electric motor housing, revealing the dominant energy transmission paths and supporting the development of tailored vibration and noise mitigation strategies.

The proposed method provides a unified, numerically robust framework for wave-based power flow analysis with clear modal interpretability, and is well suited to complex structural systems. It offers potential for applications in vibration control, energy management, and noise reduction in engineering structures.

Appendix A.

The forced response formulation for the structure shown in Fig. 2 is now derived based on the Zhong–Williams scheme. A more general expression can be derived for the propagation relation described by Eq. 62:

$$\boldsymbol{b}_i = \boldsymbol{\eta}_i \boldsymbol{b}_2 + \boldsymbol{\upsilon}_i \boldsymbol{b}_1 \tag{A.1}$$

where

$$\boldsymbol{\eta}_i = \left\lfloor \begin{bmatrix} \lambda_m & \\ & \lambda_m \end{bmatrix} \right\rfloor \boldsymbol{\eta}_{i-1} - \boldsymbol{\eta}_{i-2} \tag{A.2}$$

$$\boldsymbol{\upsilon}_i = \left\lfloor \begin{bmatrix} \lambda_m & \\ & \lambda_m \end{bmatrix} \right\rfloor \boldsymbol{\upsilon}_{i-1} - \boldsymbol{\upsilon}_{i-2} \tag{A.3}$$

Note that when $i = 1$ and $i = 2$, we have

$$\begin{aligned} \boldsymbol{\eta}_1 &= 0 \quad \boldsymbol{\upsilon}_1 = \boldsymbol{I} \\ \boldsymbol{\eta}_2 &= \boldsymbol{I} \quad \boldsymbol{\upsilon}_2 = 0 \end{aligned} \tag{A.4}$$

In this manner, $\boldsymbol{\eta}_i$ and $\boldsymbol{\upsilon}_i$ can be computed numerically.

Taking Eq. 23 into account, and in a manner similar to Eq. 24, the reflection relationship between the generalized wave amplitudes $\boldsymbol{b}_{n-1}$ and $\boldsymbol{b}_n$ can be expressed as follows:

$$\boldsymbol{b}_{n-1} = \boldsymbol{R}_n^{\mathrm{Z}} \boldsymbol{b}_n \tag{A.5}$$

where

$$\boldsymbol{R}_n^{\mathrm{Z}} = -\left(\boldsymbol{A}_{\mathrm{b}} \boldsymbol{D}_{\mathrm{RL}}^{\mathrm{C}} \mathrm{Z}_{\mathrm{q}}^{\mathrm{L}}\right)^{-1} \left(\boldsymbol{A}_{\mathrm{b}} \boldsymbol{D}_{\mathrm{RR}}^{\mathrm{C}} \mathrm{Z}_{\mathrm{q}}^{\mathrm{R}} + \boldsymbol{B}_{\mathrm{b}} \mathrm{Z}_{\mathrm{q}}^{\mathrm{R}}\right) \tag{A.6}$$

Based on Eq. A.1 and Eq. A.5, the reflection relationship between the generalized wave amplitudes $\boldsymbol{b}_2$ and $\boldsymbol{b}_1$ can be expressed as:

$$\boldsymbol{b}_1 = \boldsymbol{R}_2^{\mathrm{Z}} \boldsymbol{b}_2 \tag{A.7}$$

where

$$\boldsymbol{R}_2^{\mathrm{Z}} = \left(\boldsymbol{R}_n^{\mathrm{Z}} \boldsymbol{\upsilon}_n - \boldsymbol{\upsilon}_{n-1}\right)^{-1} \left(\boldsymbol{\eta}_{n-1} - \boldsymbol{R}_n^{\mathrm{Z}} \boldsymbol{\eta}_n\right) \tag{A.8}$$

Considering the forced boundary, we can obtain

$$\boldsymbol{b}_1 = \left(\mathrm{D}_{\mathrm{LL}}^{\mathrm{C}} \mathrm{Z}_{\mathrm{q}}^{\mathrm{L}} + \mathrm{D}_{\mathrm{LR}}^{\mathrm{C}} \mathrm{Z}_{\mathrm{q}}^{\mathrm{L}} \boldsymbol{R}_2^{\mathrm{Z}}\right)^{-1} \boldsymbol{f}_{\mathrm{e}} \tag{A.9}$$

The structural transfer function obtained by Zhong-Williams scheme can be written as

$$H^{\mathrm{Z}}(i) = \mathrm{Z_q}\boldsymbol{\eta}_i\Big(\mathrm{D_{LL}^C Z_q^L}\boldsymbol{R}_2^{\mathrm{Z}} + \mathrm{D_{LR}^C Z_q^L}\big(\boldsymbol{R}_2^{\mathrm{Z}}\big)^2\Big)^{-1} + \mathrm{Z_q}\boldsymbol{\upsilon}_i\big(\mathrm{D_{LL}^C Z_q^L} + \mathrm{D_{LR}^C Z_q^L}\boldsymbol{R}_2^{\mathrm{Z}}\big)^{-1} \tag{A.10}$$

Thus far, the Zhong–Williams scheme has been independently employed, encompassing the propagation relation, generalized symplectic eigenvalues, and eigenvectors, to derive the structural transfer function, thereby avoiding the procedure described in the literature [27, 29] that involves reconstructing the wave mode vectors.

References

[1] M. Oudich, N. J. Gerard, Y. Deng, Y. Jing, Tailoring structure-borne sound through bandgap engineering in phononic crystals and metamaterials: A comprehensive review, Advanced Functional Materials 33 (2) (2023) 2206309. arXiv:https://advanced.onlinelibrary.wiley.com/doi/pdf/10.1002/adfm.202206309, doi:https://doi.org/10.1002/adfm.202206309.
URL https://advanced.onlinelibrary.wiley.com/doi/abs/10.1002/adfm.202206309

[2] S. Lin, Y. Zhang, Y. Liang, Y. Liu, C. Liu, Z. Yang, Bandgap characteristics and wave attenuation of metamaterials based on negative-stiffness dynamic vibration absorbers, Journal of Sound and Vibration 502 (2021) 116088. doi:https://doi.org/10.1016/j.jsv.2021.116088.
URL https://www.sciencedirect.com/science/article/pii/S0022460X21001607

[3] M. Mitra, S. Gopalakrishnan, Guided wave based structural health monitoring: A review, Smart Materials and Structures 25 (5) (2016) 053001. doi:10.1088/0964-1726/25/5/053001.
URL https://dx.doi.org/10.1088/0964-1726/25/5/053001

[4] Z. Yang, H. Yang, T. Tian, D. Deng, M. Hu, J. Ma, D. Gao, J. Zhang, S. Ma, L. Yang, H. Xu, Z. Wu, A review on guided-ultrasonic-wave-based structural health monitoring: From fundamental theory to machine learning techniques, Ultrasonics 133 (2023) 107014. doi:https://doi.org/10.1016/j.ultras.2023.107014.
URL https://www.sciencedirect.com/science/article/pii/S0041624X23000902

[5] W. Wang, A. Li, Y. Fan, L. Li, Detecting bolt looseness of flanged joint based on multiple-mode conversion, Structural Health Monitoring 0 (0) (0) 14759217241286443. arXiv:https://doi.org/10.1177/14759217241286443, doi:10.1177/14759217241286443.
URL https://doi.org/10.1177/14759217241286443

[6] N. Gao, Z. Zhang, J. Deng, X. Guo, B. Cheng, H. Hou, Acoustic metamaterials for noise reduction: A review, Advanced Materials Technologies 7 (6) (2022) 2100698. arXiv:https://advanced.onlinelibrary.wiley.com/doi/pdf/10.1002/admt.202100698, doi:https://doi.org/10.1002/admt.202100698.
URL https://advanced.onlinelibrary.wiley.com/doi/abs/10.1002/admt.202100698

[7] G. Liao, C. Luan, Z. Wang, J. Liu, X. Yao, J. Fu, Acoustic metamaterials: A review of theories, structures, fabrication approaches, and applications, Advanced Materials Technologies 6 (5) (2021) 2000787. arXiv:https://advanced.onlinelibrary.wiley.com/doi/pdf/10.1002/admt.202000787, doi:https://doi.org/10.1002/admt.202000787.
URL https://advanced.onlinelibrary.wiley.com/doi/abs/10.1002/admt.202000787

[8] C. Willberg, S. Duczek, J. M. Vivar-Perez, Z. A. B. Ahmad, Simulation methods for guided wave-based structural health monitoring: A review, Applied Mechanics Reviews 67 (1) (2015) 010803. arXiv:https://asmedigitalcollection.asme.org/appliedmechanicsreviews/article-pdf/67/1/010803/6074226/amr_067_01_010803.pdf, doi:10.1115/1.4029539.
URL https://doi.org/10.1115/1.4029539

[9] A. Nilsson, B. Liu, Vibro-Acoustics, Volume 2, Vol. 2, 2016. doi:10.1007/978-3-662-47934-6.

[10] H. Lamb, On waves in an elastic plate, Proceedings of the Royal Society of London. Series A, Containing Papers of a Mathematical and Physical Character 93 (648) (1917) 114–128. arXiv:https://royalsocietypublishing.org/doi/pdf/10.1098/rspa.1917.0008, doi:10.1098/rspa.1917.0008.
URL https://royalsocietypublishing.org/doi/abs/10.1098/rspa.1917.0008

[11] D. C. Gazis, Exact analysis of the plane-strain vibrations of thick-walled hollow cylinders, The Journal of the Acoustical Society of America 30 (8) (1958) 786–794. arXiv:https://pubs.aip.org/asa/jasa/article-pdf/30/8/786/18738423/786_1_online.pdf, doi:10.1121/1.1909761.
URL https://doi.org/10.1121/1.1909761

[12] O. Saito, F. Yu, Y. Okabe, Dispersion relation of lamb waves in cross-ply composite laminates using multi-layered models, Composite Structures 264 (2021) 113691. doi:https://doi.org/10.1016/j.compstruct.2021.113691.
URL https://www.sciencedirect.com/science/article/pii/S0263822321001525

[13] Q. Chen, K. Xu, D. Ta, High-resolution lamb waves dispersion curves estimation and elastic property inversion, Ultrasonics 115 (2021) 106427. doi:https://doi.org/10.1016/j.ultras.2021.106427.
URL https://www.sciencedirect.com/science/article/pii/S0041624X21000664

[14] M. Rabbi, K. Teramoto, H. Ishibashi, M. Roshid, Imaging of sub-surface defect in cfrp laminate using a0-mode lamb wave: Analytical, numerical and experimental studies, Ultrasonics 127 (2023) 106849. doi:https://doi.org/10.1016/j.ultras.2022.106849.
URL https://www.sciencedirect.com/science/article/pii/S0041624X2200155X

[15] A. W. Leissa, Vibration of Shells, Acoustical Society of America, New York, 1993.

[16] M. Mirzaei, Y. Kiani, Free vibration of functionally graded carbon nanotube reinforced composite cylindrical panels, Composite Structures 142 (2016) 45–56. doi:https://doi.org/10.1016/j.compstruct.2015.12.071.
URL https://www.sciencedirect.com/science/article/pii/S0263822316000799

[17] W. Liang, T. Liu, C. Li, Q. Wang, Three-dimensional vibration model of cylindrical shells via carrera unified formulation, Materials 16 (9) (2023). doi:10.3390/ma16093345.
URL https://www.mdpi.com/1996-1944/16/9/3345

[18] B. R. Mace, E. Manconi, Modelling wave propagation in two-dimensional structures using finite element analysis, Journal of Sound and Vibration 318 (4) (2008) 884–902.

doi:https://doi.org/10.1016/j.jsv.2008.04.039.
URL https://www.sciencedirect.com/science/article/pii/S0022460X0800391X

[19] C. W. Zhou, J. P. Lainé, M. N. Ichchou, A. M. Zine, Wave finite element method based on reduced model for one-dimensional periodic structures, International Journal of Applied Mechanics 07 (02) (2015) 1550018. arXiv:https://doi.org/10.1142/S1758825115500180, doi:10.1142/S1758825115500180.
URL https://doi.org/10.1142/S1758825115500180

[20] L. Li, Z. Jiang, Y. Fan, J. Li, Creating the coupled band gaps in piezoelectric composite plates by interconnected electric impedance, Materials 11 (9) (2018). doi:10.3390/ma11091656.
URL https://www.mdpi.com/1996-1944/11/9/1656

[21] J.-M. Mencik, M. Ichchou, Multi-mode propagation and diffusion in structures through finite elements, European Journal of Mechanics - A/Solids 24 (5) (2005) 877–898. doi:https://doi.org/10.1016/j.euromechsol.2005.05.004.
URL https://www.sciencedirect.com/science/article/pii/S0997753805000665

[22] D. Mead, Wave propagation and natural modes in periodic systems: I. mono-coupled systems, Journal of Sound and Vibration 40 (1) (1975) 1–18. doi:https://doi.org/10.1016/S0022-460X(75)80227-6.
URL https://www.sciencedirect.com/science/article/pii/S0022460X75802276

[23] D. Mead, Wave propagation and natural modes in periodic systems: Ii. multi-coupled systems, with and without damping, Journal of Sound and Vibration 40 (1) (1975) 19–39. doi:https://doi.org/10.1016/S0022-460X(75)80228-8.
URL https://www.sciencedirect.com/science/article/pii/S0022460X75802288

[24] J.-M. Mencik, New advances in the forced response computation of periodic structures using the wave finite element (wfe) method, Computational Mechanics 54 (09 2014). doi:10.1007/s00466-014-1033-1.

[25] W. Zhong, F. Williams, On the direct solution of wave propagation for repetitive structures, Journal of Sound and Vibration 181 (3) (1995) 485–501. doi:https://doi.org/10.1006/jsvi.1995.0153.
URL https://www.sciencedirect.com/science/article/pii/S0022460X85701538

[26] W. Zhong, F. Williams, Wave problems for repetitive structures and symplectic mathematics, Proceedings of the Institution of Mechanical Engineers, Part C: Journal of Mechanical Engineering Science 206 (6) (1992) 371–379.

[27] Y. Waki, B. Mace, M. Brennan, Numerical issues concerning the wave and finite element method for free and forced vibrations of waveguides, Journal of Sound and Vibration 327 (1) (2009) 92–108. doi:https://doi.org/10.1016/j.jsv.2009.06.005.
URL https://www.sciencedirect.com/science/article/pii/S0022460X09004908

[28] Y. Fan, M. Collet, M. Ichchou, L. Li, O. Bareille, Z. Dimitrijevic, Enhanced wave and finite element method for wave propagation and forced response prediction in periodic piezoelectric structures, Chinese Journal of Aeronautics 30 (1) (2017) 75–87. doi:https://doi.org/10.1016/j.cja.2016.12.011.
URL https://www.sciencedirect.com/science/article/pii/S1000936116302308

[29] W. Wang, Y. Fan, L. Li, Extending zhong-williams scheme to solve repeated-root wave modes, Journal of Sound and Vibration 519 (2022) 116584. doi:https://doi.org/10.1016/j.jsv.2021.116584.
URL https://www.sciencedirect.com/science/article/pii/S0022460X21006015

[30] D. Mead, Waves and modes in finite beams: Application of the phase-closure principle, Journal of Sound and Vibration 171 (5) (1994) 695–702. doi:https://doi.org/10.1006/jsvi.1994.1150.
URL https://www.sciencedirect.com/science/article/pii/S0022460X84711503

[31] D. Duhamel, B. Mace, M. Brennan, Finite element analysis of the vibrations of waveguides and periodic structures, Journal of Sound and Vibration 294 (1) (2006) 205–220. doi:https://doi.org/10.1016/j.jsv.2005.11.014.
URL https://www.sciencedirect.com/science/article/pii/S0022460X05007194

[32] J.-M. Mencik, D. Duhamel, A wave-based model reduction technique for the description of the dynamic behavior of periodic structures involving arbitrary-shaped substructures and large-sized finite element models, Finite Elements in Analysis and Design 101 (2015) 1–14. doi:https://doi.org/10.1016/j.finel.2015.03.003.
URL https://www.sciencedirect.com/science/article/pii/S0168874X15000426

[33] D. Duhamel, J.-M. Mencik, Time response analysis of periodic structures via wave-based absorbing boundary conditions, European Journal of Mechanics - A/Solids 91 (2022) 104418. doi:https://doi.org/10.1016/j.euromechsol.2021.104418.
URL https://www.sciencedirect.com/science/article/pii/S099775382100173X

[34] D. Duhamel, J.-M. Mencik, Reduced-order modeling for time domain analysis of finite periodic structures with absorbing boundary conditions, Journal of Sound and Vibration 590 (2024) 118576. doi:https://doi.org/10.1016/j.jsv.2024.118576.
URL https://www.sciencedirect.com/science/article/pii/S0022460X24003390

[35] M. Ichchou, J.-M. Mencik, W. Zhou, Wave finite elements for low and mid-frequency description of coupled structures with damage, Computer Methods in Applied Mechanics and Engineering 198 (15) (2009) 1311–1326. doi:https://doi.org/10.1016/j.cma.2008.11.024.
URL https://www.sciencedirect.com/science/article/pii/S0045782508004209

[36] W. Zhou, M. Ichchou, Wave scattering by local defect in structural waveguide through wave finite element method, Structural Health Monitoring 10 (4) (2011) 335–349. arXiv:https://doi.org/10.1177/1475921710373431, doi:10.1177/1475921710373431.
URL https://doi.org/10.1177/1475921710373431

[37] Y. Fan, C. Zhou, J. Laine, M. Ichchou, L. Li, Model reduction schemes for the wave and finite element method using the free modes of a unit cell, Computers & Structures 197 (2018) 42–57.

[38] T. L. Huang, M. N. Ichchou, O. A. Bareille, Multi-mode wave propagation in damaged stiffened panels, Structural Control and Health Monitoring 19 (5) (2012) 609–629. arXiv:https://onlinelibrary.wiley.com/doi/pdf/10.1002/stc.451, doi:https://doi.org/10.1002/stc.451.
URL https://onlinelibrary.wiley.com/doi/abs/10.1002/stc.451

[39] W. Zhou, M. Ichchou, J. Mencik, Analysis of wave propagation in cylindrical pipes with local inhomogeneities, Journal of Sound and Vibration 319 (1) (2009) 335–354. doi:https://doi.org/10.1016/j.jsv.2008.05.039.
URL https://www.sciencedirect.com/science/article/pii/S0022460X08005130

[40] J. M. Renno, B. R. Mace, Vibration modelling of structural networks using a hybrid finite element/wave and finite element approach, Wave Motion 51 (4) (2014) 566–580, innovations in Wave Modelling. doi:https://doi.org/10.1016/j.wavemoti.2013.09.001.
URL https://www.sciencedirect.com/science/article/pii/S0165212513001455

[41] Y. Fan, M. Collet, M. Ichchou, L. Li, O. Bareille, Z. Dimitrijevic, Energy flow prediction in built-up structures through a hybrid finite element/wave and finite element approach, Mechanical Systems and Signal Processing 66-67 (2016) 137–158. doi:https://doi.org/10.1016/j.ymssp.2015.05.014.
URL https://www.sciencedirect.com/science/article/pii/S0888327015002356

[42] B. MACE, P. SHORTER, Energy flow models from finite element analysis, Journal of Sound and Vibration 233 (3) (2000) 369–389. doi:https://doi.org/10.1006/jsvi.1999.2812.
URL https://www.sciencedirect.com/science/article/pii/S0022460X99928122

[43] R. R. Craig Jr, M. C. Bampton, Coupling of substructures for dynamic analyses., AIAA journal 6 (7) (1968) 1313–1319.

[44] J.-M. Mencik, Improved model reduction with basis enrichment for dynamic analysis of nearly periodic structures including substructures with geometric changes, Journal of Computational and Applied Mathematics 445 (2024) 115844. doi:https://doi.org/10.1016/j.cam.2024.115844.
URL https://www.sciencedirect.com/science/article/pii/S0377042724000931

[45] F. Bloch, Über die quantenmechanik der elektronen in kristallgittern, Zeitschrift für physik 52 (7) (1929) 555–600.

[46] D. Bestle, Eigenvalue sensitivity analysis based on the transfer matrix method, International Journal of Mechanical System Dynamics 1 (1) (2021) 96–107. arXiv:https://onlinelibrary.wiley.com/doi/pdf/10.1002/msd2.12016, doi:https://doi.org/10.1002/msd2.12016.
URL https://onlinelibrary.wiley.com/doi/abs/10.1002/msd2.12016

[47] M. Ling, L. Yuan, H. Zhou, M. Ning, Modified transfer matrix method for vibration analysis of beam structures including branches and rigid bodies, Mechanical Systems and Signal Processing 187 (2023) 109858.

doi:https://doi.org/10.1016/j.ymssp.2022.109858.
URL https://www.sciencedirect.com/science/article/pii/S0888327022009268